

# Journal Pre-proof

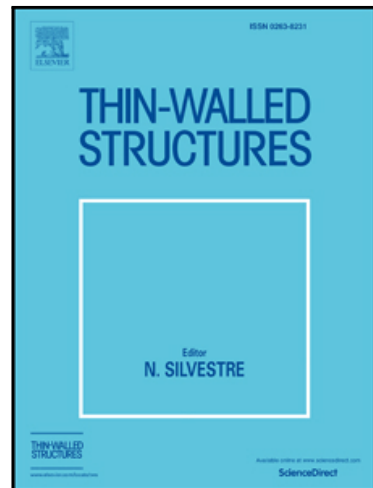
A flexible design framework for lattice-based chiral mechanical metamaterials considering dynamic energy absorption

Weiyun Xu , Chang Zhou , Hanyu Zhang , Zhao Liu , Ping Zhu

PII: S0263-8231(24)00550-0

DOI: <https://doi.org/10.1016/j.tws.2024.112108>

Reference: TWST 112108



To appear in: *Thin-Walled Structures*

Received date: 5 January 2024

Revised date: 30 April 2024

Accepted date: 7 June 2024

Please cite this article as: Weiyun Xu , Chang Zhou , Hanyu Zhang , Zhao Liu , Ping Zhu , A flexible design framework for lattice-based chiral mechanical metamaterials considering dynamic energy absorption, *Thin-Walled Structures* (2024), doi: <https://doi.org/10.1016/j.tws.2024.112108>

This is a PDF file of an article that has undergone enhancements after acceptance, such as the addition of a cover page and metadata, and formatting for readability, but it is not yet the definitive version of record. This version will undergo additional copyediting, typesetting and review before it is published in its final form, but we are providing this version to give early visibility of the article. Please note that, during the production process, errors may be discovered which could affect the content, and all legal disclaimers that apply to the journal pertain.

© 2024 Published by Elsevier Ltd.

**Highlights**

- Flexible framework for chiral mechanical metamaterial with various configurations.
- An integration of joint enhancement design, bio-inspired helical design, and gradient design.
- A general characterization method of chiral geometrical features.
- FEA and experiments of uniaxial medium-strain-rate ( $50\text{ s}^{-1}$ ) compression were conducted.
- The proposed bidirectional gradient design achieves a 52.0 % specific energy absorption enhancement.

# A flexible design framework for lattice-based chiral mechanical metamaterials considering dynamic energy absorption

Weiyun Xu<sup>1</sup>, Chang Zhou<sup>1</sup>, Hanyu Zhang<sup>1, #</sup>, Zhao Liu<sup>2, #</sup>, Ping Zhu<sup>1, #</sup>

<sup>1</sup> The State Key Laboratory of Mechanical System and Vibration, National Engineering Research Center of Automotive Power and Intelligent Control, School of Mechanical Engineering, Shanghai Jiao Tong University, Shanghai, China.

<sup>2</sup> School of Design, Shanghai Jiao Tong University, Shanghai, China.

<sup>#</sup> Correspondence to Ping Zhu ([pzhu@sjtu.edu.cn](mailto:pzhu@sjtu.edu.cn)), Zhao Liu ([hotlz@sjtu.edu.cn](mailto:hotlz@sjtu.edu.cn)), and Hanyu Zhang ([zhanghanyu@sjtu.edu.cn](mailto:zhanghanyu@sjtu.edu.cn)).

**Abstract** While chiral mechanical metamaterials (CMMs) are reported promising in energy absorption due to the unique chiral effect, the energy-absorbing CMMs lack effective and generalized design methodologies and corresponding structure-property relationship studies. To this end, a design framework for lattice-based CMMs was proposed, and the dynamic compressive behaviors of CMMs were systematically investigated. Firstly, based on a predefined design baseline that considered a support-free metal additive manufacturing process, a screw-theory-based assembly rule was presented, which enabled the scalable twist effects and the characterization of chiral features. Secondly, an aperiodic design process that sequentially defines joints, strut connections, and geometrical features was proposed. This framework via parameterization enables the rapid generation of geometric and finite element models that contain a large number of unit cells. It also enables the integration of joint enhancement design, bio-inspired helical design, and gradient design. Finally, by finite element analysis and experiments of uniaxial medium-strain-rate ( $50\text{ s}^{-1}$ ) compression, the effects of chirality on mechanical properties (compressive strength, yield plateau, energy absorption, etc.) during the nonlinear large-deformation responses were elucidated. Results show that a comprehensive and flexible method is presented by independently defining each rod component or joint of the lattice type metamaterials, which enables the design from chiral to achiral, from rectangular to helical, and from uniform to gradient. The bidirectional gradient CMMs design along the axial and radial directions achieves a 52.0 % specific energy absorption enhancement compared with achiral lattices, demonstrating the energy absorption advantage of CMMs, and laying the foundation for further optimization, inverse design, and engineering applications.

**Keywords** Mechanical metamaterial, Chiral, Dynamic compression, Energy absorption, Gradient design, 3D printing

## 1. Introduction

The applications of lightweight materials or structures with energy-absorbing, impact-resistant capabilities are commonly emphasized in the aerospace, marine, and automotive fields [1-4]. In recent years, mechanical metamaterials (MMs), type of which includes lattice [5], plate lattice [6], triply periodic minimal surface (TPMS) [7], etc., have been favored in crashworthiness studies due to their customizable geometry and multi-material printing capabilities conferred by additive manufacturing (AM) [8,9]. By designing unit-cell microstructures of metamaterials, scholars have enabled greater design freedom for energy-absorptive metamaterials than traditional honeycomb or porous structures, which in turn has allowed them to modulate the mechanical properties of MMs and realize the design from isotropic materials to anisotropic, heterogeneous, and multiscale ones [10-13].

One of these design approaches includes the introduction of chiral features to capture the coupled deformation modes of compression-to-torsion that are not present in conventional homogeneous materials as assumed by Cauchy's elastomer [14,15]. This unique deformation mode is known as the twist effect or chiral effect, and the metamaterials are referred to as chiral mechanical metamaterials (CMMs). Via the symmetry-broken chiral architectures, the twist effect obtained in CMMs mirrors the twist phenomenon in nature that facilitates structural stability and toughness. For example, the left-handed/right-handed towel gourd tendrils [16], the twist-tension coupling in DNA structures [17], humidity-driven spider silks [18], and helicoidal (Bouligand) structures in beetle elytron and crab [19]. Typically, to describe the translation-rotation coupling behavior of CMMs, the twist deformation of chiral configuration can be characterized as the motion along rotation degrees of freedom (DOF) and then be analyzed using mechanism-based methods [20,21]. And the corresponding mechanical properties (Young's modulus, Poisson's ratio, twist angle per uniaxial strain, etc.) are often mapped onto micropolar or Cosserat continuum elasticity [21,22], which assumes additional rotation DOF for every particle of the bulk. However, the constitutive equations require the introduction of much more elastic constants (e.g., for cubic symmetric CMMs the number is twelve [23]) in order to establish the equilibrium of the stresses and stress moments, respectively. Not to mention that this constitutive model is within the linear elastic range and the unit cells need to satisfy periodic boundary conditions.

Researches on energy-absorbing performance of chiral mechanical metamaterials have shown the advantages of this light-weight material in terms of wave propagation, buffering, and shock absorption [22,24,25]. The deformation characteristics of CMMs can be sorted as bending-dominated according to M. F. Ashby's analysis on lattices [26], which are suitable for energy absorption. During the compression process caused by uniaxial load, CMMs is able to convert and dissipate more energy via the elastic and plastic bending of diagonal rods that make up the chiral unit cell, and the contact and friction either among these rods or between adjacent unit cells as the compression-to-torsion deformation goes on [27,28]. Compared to typical lattices, the material is pressed and twisted at the same time, which is more conducive to the compressive stability [29]. Moreover, there exist some types of CMMs with zero or negative Poisson's ratio, a beneficial property for crashworthiness that has been widely used in recent years [30-32]. All these explain the underlying mechanisms of CMMs for a good energy-absorbing capability. To investigate the mechanical properties of CMMs considering the large deformation and nonlinearity during compression, the research tools are generally finite element analysis (FEA) and experimental validation. Nevertheless, quasi-static conditions are often conducted while dynamic tests are rare.

With the aforementioned prospect, various categories of chiral unit cells have been proposed enabling a flexible design of CMMs, e.g., Z-shaped [33], O-shaped [34], and #-shaped [35] metamaterials. Most of the chiral materials and structures are artificially and rationally designed based on the insights obtained from bionics or topology optimization [36-38], which hinders the generalization of methods to one another and makes it difficult to develop a unified characterization of the various chiral geometries. Not to mention that, the further research on the structure-property relationship between the designed geometry and the energy absorption would bring more challenges. Meanwhile, compared to two-dimensional (2D) metamaterials, three-dimensional (3D) ones most of which are assembled by 2D motifs [39-41] have more practical applications. However, due to the difficulties brought by the support removal and accuracy of additive manufacturing (AM) processes, few designs have been reported with many unit cells aligned along the printing direction. This makes material properties significantly affected by boundary effects and hinders the application to large metamaterial systems where there is a large number of unit cells [42]. Last but not least, the unscalable twist effect of periodic CMMs, which greatly diminishes the twist angle as the number of unit cells multiplies, also prevents CMMs from exhibiting unique mechanical behavior in large metamaterial system [43,44]. Therefore, it is necessary to investigate design methods for chiral metamaterials that consider manufacturability and as well achieve a scalable twist effect.

Last but not least, bio-inspired design is a proven method to enhance the cushioning and energy absorption properties of metamaterials [45-47]. Recently, a large number of biomimetic metamaterial designs have been developed, e.g., bamboo tube [48], spiderweb honeycomb [49], bone cellular foam[50]. Typically, bio-inspired structures have excellent performance due to the utilization of materials and structural arrangement [51]. For example, as a representative strategy in nature, Bouligand structures consisting of twistedly arranged sheets of nanofibers are widely found in clubs, scales, bones of stomatopods and in the exoskeletons of crustaceans [52]. Bouligand structures are characterized by the absorption of energy by rotating and repositioning ordered nanofibers under external loading [53]. Gradient design is also a representative strategy for damage-resistant biological structures which are both strong and tough without performance mismatches [8]. And studies on an in-plane gradient core of sandwich structure or an out-of-plane gradient crush box [1,54] have reported an effective improvement on mechanical behaviors via this bio-inspired design. Currently, there are few reports on the bio-inspired design applied to chiral mechanics metamaterials, and the cushioning and energy-absorbing mechanisms underlying the structural design need to be further investigated.

Facing the gaps in terms of the characterization, mechanical properties, and design methods of chiral mechanical metamaterials, this study aims to reveal the impact of the deformation mechanism of CMMs on energy absorption, to explore the inherent connection between the mechanism and the design comprehensively, and thus to obtain better energy-absorbing properties by modified designs. Consequently, a design framework for lattice-based CMMs that enables scalable twist effects was proposed. Different chiral configurations can be generated efficiently and effectively and then be characterized. The selective laser melting (SLM) technique was utilized to fabricate 316L metal CMMs samples and conducted medium-strain-rate dynamic compressions to test the corresponding properties. A joint-enhanced design, a bio-inspired helical design, and a bi-directional gradient design were also integrated into this framework, and their respective effects on improving the non-linear crush behaviors were discussed. By parameterization, computer-aided design (CAD) and finite element analysis (FEA) models can be generated rapidly under a vast design space. Not only that, the underlying deformation mechanisms of the designed CMMs and structure-property relationships were further elucidated. Results showed a significant improvement of energy absorption compared with achiral metamaterials. With the insights obtained from the design method and results in this work, the crashworthiness of CMMs can be further optimized and then applied to automobile crush box, aircraft sandwich bulkhead, protective clothing, and so on.

This article was developed as follows. In Section 2, the proposed design framework of chiral mechanical metamaterials was introduced. The assembly rules were explained, and the design parameters of every modified design were illustrated. The settings of AM, FEA, and experiments were also introduced including the constitutive model of material, the meshing method, the boundary conditions, etc. In Section 3, the characterization method of chirality was illustrated, and the deformation and failure modes of the proposed CMMs were analyzed by comparing the mechanical responses of various chiral configurations. After that, the effect of geometric parameters on impact-resistance was quantified and illustrated. The advantages of our method were discussed. Following that, conclusions were drawn in Section 4.

## 2. Materials and methods

In this section, the proposed design framework for CMMs was introduced. The basic lattices-based design is illustrated, along with the settings of constituent material and SLM manufacturing process. Utilizing screw theory, the assembly rules enabling scalable twist effect were established. And the modified design methods by enhancing joints, helix, and gradient were thereafter introduced to form the comprehensive parameterization design. Following that, the FEA and experimental settings of dynamic compression were presented.

### 2.1. Basic design and manufacturing of chiral mechanical metamaterials

**2.1.1. Geometrical features considering additive manufacturing.** As shown in Fig. 1, a CMMs design workflow considering manufacturability of AM and scalable twist effect is constructed. Given that most CMMs are lattice type which is composed of rod structures [33-35,39], the classical Z-shaped motif is selected as the basic geometry in this study. The reason is that, 3D Z-shaped structure is the simplest chiral structure which can rotate in response to uniaxial compression and can have larger twist angle compared with other chiral types such as O-shaped and #-shaped structures [14]. With the size of  $a_x \times a_y \times a_z$  and rod diameter of  $d$ , the Z-shaped unit cell is assembled by a 90° central-symmetrical arrangement of the 2D motif along its central axis in z-direction. Then, the unit cell is periodically aligned along three principal directions

with number  $N_x$ ,  $N_y$ , and  $N_z$  respectively, and z-direction is defined as the direction of twist, as shown in Fig. 1(a). In this way, the  $N_x \times N_y \times N_z$  chiral structure can be divided into  $n$  layers along z-direction where  $n = N_z$ .

SLM was used to manufacture the metal CMMs samples for further energy-absorbing tests, with the z-direction as the printing direction. All columnar samples were manufactured by a metal 3D printer - 3D Systems DMP 320 (Fig. 1b). AISI 316L stainless steel was selected as the constituent material of the printing for its good ductility and toughness, which is suitable for the crashworthiness study of CMMs. According to the SLM manufacturer, the chemical composition and physical parameters of SLM 316L, and the AM process parameters are listed in Appendix A.1.

Although manufacturing process is not a focus of this work, a reliable 3D-printing fabrication quality of chiral metamaterials is an essential prerequisite for the later experimental validation in this paper. More importantly, the design for additive manufacturing (AM) of CMMs should be stressed to ensure a support-free 3D printing of large metamaterial system. Hence, the manufacturable geometrical parameters were pre-tested by printing a batch of strut samples that varied in diameter, cross section shape, and inclined angle, as shown in Fig. 1(c). By detecting the forming quality and avoiding obvious printing defect, this procedure enables the reliable fabrication of CMMs samples and serves as the guideline to construct the strut design domain in Fig. 1(d). As a result, the rod diameter is set greater than 0.5 and the inclination angle of diagonal strut is larger than  $18^\circ$  in the design method presented later in this work. Meanwhile, the geometry of original CMMs was adapted to suit the manufacturing constraints by canceling all the transverse struts (the crossbars of the Z-shaped unit cell) and adding the vertical struts instead as shown in Fig. 1(e), which enabled the self-support design for metal SLM.

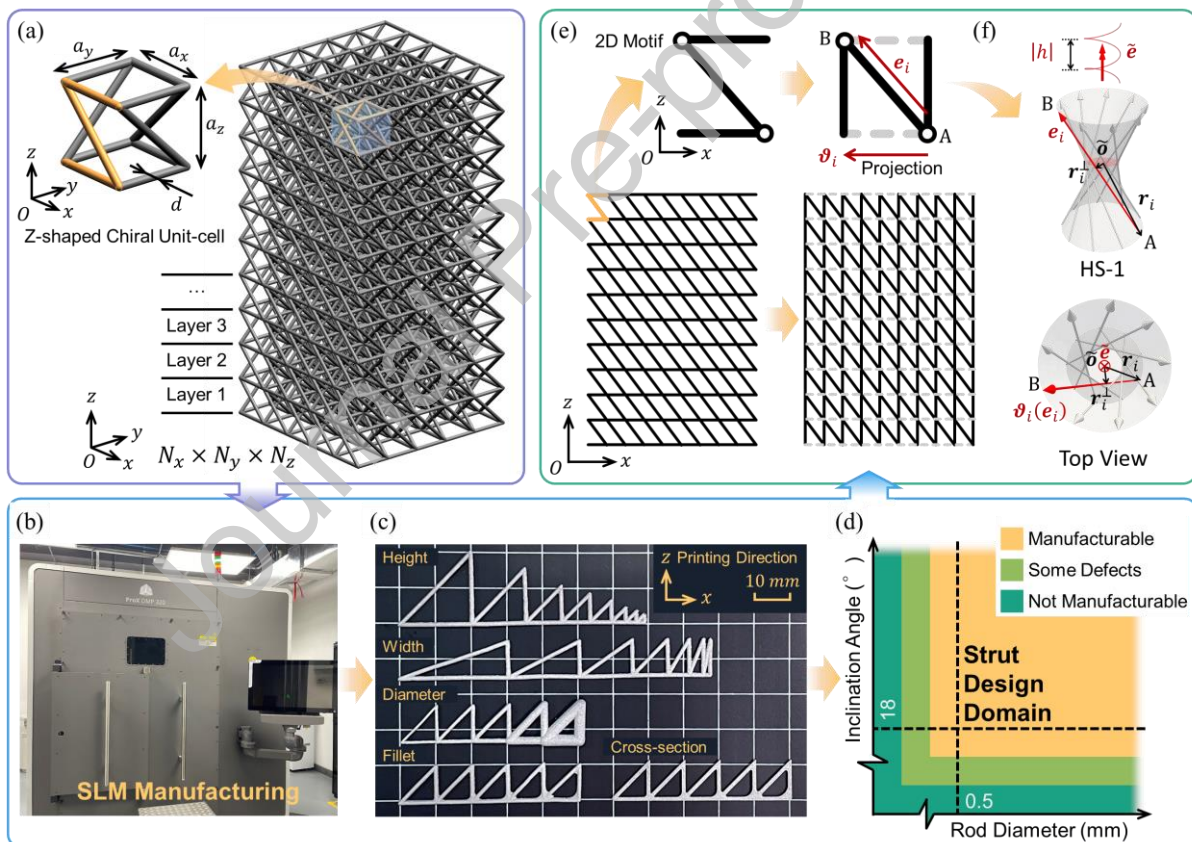


**Fig. 1. The basic geometry of chiral mechanical metamaterials emphasizing manufacturability and scalable twist effect.** (a) Original CMMs crystal arranged periodically by the Z-shaped unit cell. (b) The metal SLM machine ProX-DMP320 used in this work. (c) The fabricated strut structures to pre-test the manufacturable geometrical parameters. (d) The basic design domain constructed by feasible intervals of the rod diameter and the inclination angle. (e) The side views of the lattice-based CMMs before and after modification that enables self-support printing, and the corresponding instant pseudo-rigid body models (PRBM) of 2D Z-shaped motifs. (f) The HS-1 constraint screw characterizing the motion of the left-handed chiral base structures.

**2.1.2. Assembly rules based on screw theory.** To obtain observable twist angles of CMMs even when the total number of unit cells is large, e.g.,  $N_x \times N_y \times N_z > 10^3$ , our screw-theory-based method that can

achieve scalable twist effect [33] is applied, which helps to take full advantage of the tension-torsion coupling deformation behavior to absorb energy. According to the screw theory [55], a screw representation can well describe the compression-to-rotation deformation of chiral unit cell by a translational component along and a rotational component around an instantaneous screw axis (ISA). This enables the use of rigorous algebraic theory to analyze the instant behaviors of CMMs assembled by multiple unit cells.

Specifically, as illustrated in Fig. 1(e), a 3D unit cell with twist effects can be further disassembled into 2D base structures – the Z-shaped motif in this case. Thus, each base structure can be modelled as an instant pseudo-rigid body (PRBM) [28,39] and the corresponding DOF can be described using screw representations. The DOF of an instant PRBM can be described by a motion screw  $\xi = \omega[\tilde{\mathbf{e}}, h\tilde{\mathbf{e}}]^T$  with an angular velocity  $\omega$ , a finite pitch  $h$ , and the center line  $\tilde{\mathbf{e}}$  as its ISA. The constraints within the unit cell can also be described by a set of constraint screws  $\{\zeta_i\}$  with ISA  $\mathbf{e}_i$  which is shown in Fig. 1(f). Our investigation [33] has previously elucidated that, to achieve the twist DOF  $\xi$ , ISA  $\mathbf{e}_i$  of each constraint  $\zeta_i$  should belong to the same branch of straight lines on a hyperbolic surface of one sheet (HS-1) centering around  $\tilde{\mathbf{e}}$ , i.e.,  $\zeta_i = [\mathbf{e}_i, \mathbf{r}_i \times \mathbf{e}_i]^T$ , where  $\mathbf{r}_i$  is a vector connecting the unit-cell center  $\tilde{\mathbf{o}}$  and a point on ISA. By requiring  $\tilde{\mathbf{e}} \cdot \mathbf{e}_i > 0$ , the sign of  $\tilde{\mathbf{e}} \cdot \mathbf{r}_i \times \mathbf{e}_i$  can be used to differentiate the two branches of straight lines on HS-1, which should be the same for all  $\zeta_i$ . The pitch of  $\xi$  can be obtained as

$$h = \frac{-\tilde{\mathbf{e}} \cdot (\mathbf{r}_i \times \mathbf{e}_i)}{\tilde{\mathbf{e}} \cdot \mathbf{e}_i} = \frac{\mathbf{r}_i^\perp \cdot (\tilde{\mathbf{e}} \times \mathbf{e}_i)}{\tilde{\mathbf{e}} \cdot \mathbf{e}_i} \quad (1)$$

where  $\mathbf{r}_i^\perp = r\mathbf{e}_{r,i}$  is the vector starting from  $\tilde{\mathbf{o}}$  and perpendicularly connecting to the ISA of  $\zeta_i$ , with a length of  $r$ . Based on the analysis, it can be obtained that the compatible chirality of CMMs which enables scalable twist effects requires a share screw for all its unit cells, i.e., all unit cells have the same center line  $\tilde{\mathbf{e}}$ , pitch  $h$ , and the branch of HS-1  $\text{sgn}(h)$ . Considering the geometrical features, the proposed CMMs can be viewed as wrapped up around  $\tilde{\mathbf{e}}$  layer by layer, and define that the pitch in the  $k$ -th layer, i.e.,  $h^k$ , is equal everywhere in this layer, as demonstrated by the top views of CMMs in Fig. 2. Referring to Eq. (1), this “isopitch” design makes the unit cells, which were equal in size in original design, become unequal, i.e.,  $\mathbf{l}^k = (l_m^k), m = 1, 2, \dots, k$ .

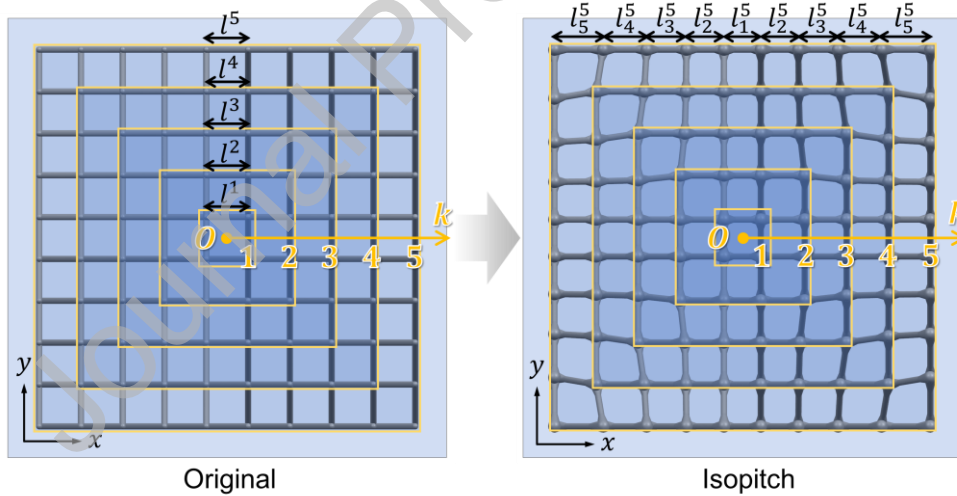


**Fig. 2. Isopitch design: adjusting the size of the unit cell so that the pitch of each layer is equal everywhere in this layer.** The figure shows the top view of the CMMs proposed in Fig. 1(a) with  $N_x = N_y = 9$ . So, the number of layers  $k = (N_x + 1)/2 = 5$ . Noted that  $k = N_x/2$  if  $N_x$  even. In the original design, all unit cells obey a periodic arrangement and are equal in size. While in isopitch design, the side length forms an array  $\mathbf{l}^k$  in order to follow Eq. (1).

Thus, an aperiodic assembly rule  $A(\mathbf{r}_i, \mathbf{e}_i, h^k)$  was presented for each diagonal strut to ensure a scalable twist effect of CMMs. Given the predefined center line  $\tilde{\mathbf{e}}$ , the criteria can be expressed as

$$\text{sgn}(\tilde{\mathbf{e}} \cdot \mathbf{r}_i \times \mathbf{e}_i) = \begin{cases} +1, \text{right handedness} \\ 0, \text{irrotation} \\ -1, \text{left handedness} \end{cases} \quad (2)$$

$$h^k \equiv \text{constant}, k = 1, 2, 3, \dots, (N_x + 1)/2 \quad (3)$$

where  $\mathbf{e}_i$  represents the orientation vector of arbitrary diagonal strut (rod AB in Fig. 1e) within each Z-shaped unit cell and  $\mathbf{r}_i$  is the position vector of the strut end point that guarantees  $\tilde{\mathbf{e}} \cdot \mathbf{e}_i > 0$ . It should be noted that, this rule is applicable to various types of CMMs unit cell including O-shaped and #-shaped CMMs [33], which makes the proposed design method versatile.

## 2.2. Aperiodic framework of chiral mechanical metamaterials

In accordance to Eq. (2), a unified chirality configuration can be generated if all chiral base structures are compatible with one another in the handedness. To satisfy the compatibility, it breaks the periodic configuration of the original CMMs design. And the unified CMMs can be transformed into a mixed configuration by defining opposite handedness within different layers along z-direction. Moreover, the handedness of each base structure can be assigned independently, which provides a vast design domain with diverse combinations of chiral geometry and handedness. Based on the insight, the aperiodic characteristics were further adopted to the geometrical parameters, which formed a design framework as illustrated in Fig. 3.

In this design method, the lattice-based CMMs are deconstructed as joints and rod components instead of unit cells to fully utilize the flexibility of aperiodic definition. Specifically, this method is divided into three steps: seeding, connecting, and enhancing. Firstly, in the seeding step as shown in Fig 3(a), the size and location of each spherical joint – the geometry that connect the ends of struts – can be independently defined within the space occupied by the overall size of CMMs crystals. The  $i$ -th,  $j$ -th, and  $k$ -th joint along  $x$ -axis,  $y$ -axis, and  $z$ -axis respectively is denoted as  $J_{i,j,k}$ . And the number of joints  $(N_x + 1) \times (N_y + 1) \times (N_z + 1)$  corresponds to that of unit cells, i.e.,  $N_x \times N_y \times N_z$ . If the distance between adjacent joints varies for different locations, it can intuitively form an uneven distribution such as graded or disordered configuration. Conversely with the same distance, a unified distribution is generated, as shown in Fig. 3(a). Next in connecting step, the connect relationships between joints can be defined according to the chiral configuration of CMMs. As mentioned in Section 2.1, the rods contain vertical struts for self-support printing and diagonal struts for twist effect. The handedness of diagonal strut is determined according to the proposed assembly criteria  $A(\mathbf{r}_i, \mathbf{e}_i, h^k)$ , contributing to the overall chirality, as illustrated in Fig. 3(b). Finally in enhancing step, the geometric details of CMMs are defined or refined in order to change the corresponding mechanical properties. The means include reinforcing the joints using fillet geometry, helical twisting of the overall macrostructure, localized refinement of the rod diameter, etc., which will be described in detail after. In this way, a design process that sequentially defines joints, defines strut connections, and refines features is proposed, enabling a comprehensive parameterization modeling method for lattice-based metamaterials.

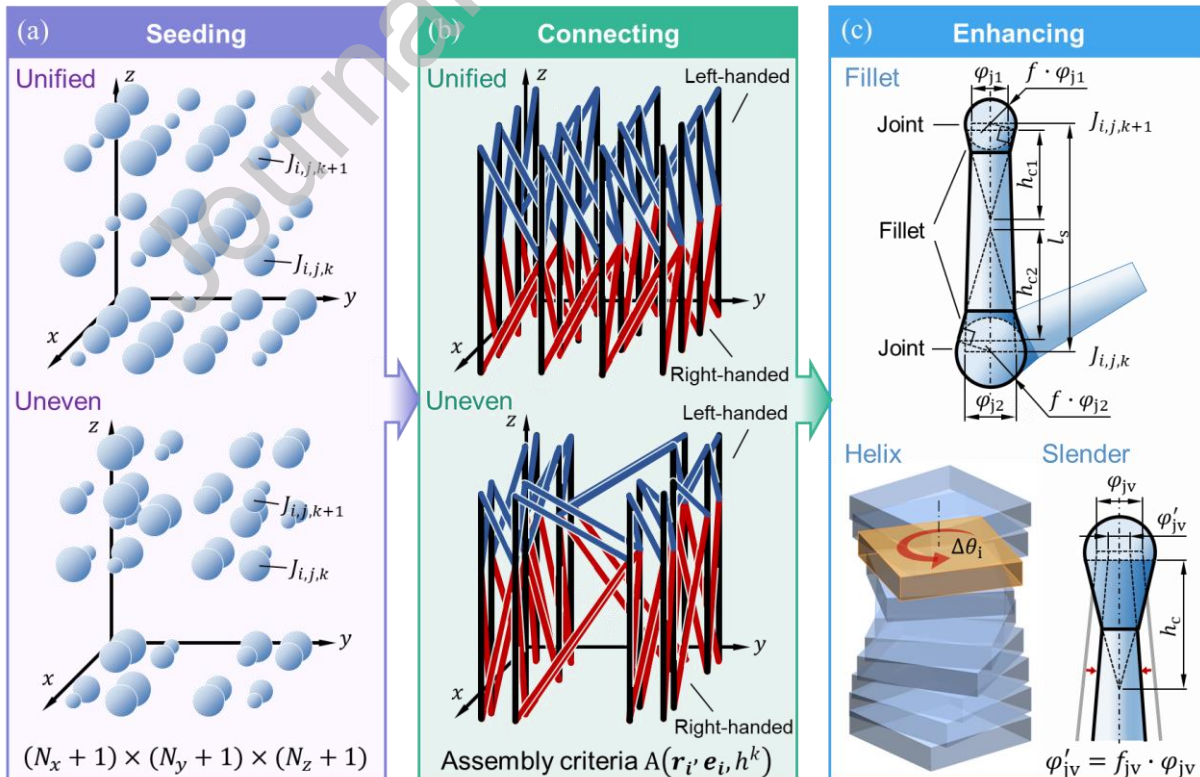


**Fig. 3. Aperiodic design framework of chiral mechanical metamaterials.** (a) Seeding step where the size and location of each spherical joint are defined. (b) Connecting step to connect the joints by rod components according to the proposed assembly rules. The black bold lines indicate the vertical struts while the blue and red ones are the diagonal struts. (c) Enhancing step including joint-enhancing, helix, and slenderness of strut.

**2.2.1. Joint-enhanced design based on rigidity theory.** Generally, lattice metamaterials experience concentrated stresses at the joints during plastic deformation, causing plastic hinges and premature destructive failure thus affecting their energy-absorbing properties [56,57]. Therefore, designs have been proposed to reduce the stress concentration and improve the rigidity and strength of lattice material by enhancing the joints by fillet-like geometric transition from joints to struts [58,59]. Herein, a joint-enhanced design under the proposed framework was also introduced, as shown in Fig. 3(c).

With the geometric parameters of the joints and the connecting information defined, the geometry of enhanced joint under arbitrary CMMs configuration can be generated. Specifically, if the connected joints ( $J_{i,j,k}$  and  $J_{i,j,k+1}$ ) have the same diameter, i.e.,  $\varphi_{j1} = \varphi_{j2} = \varphi$ , the strut is defined as a cylinder with diameter  $\varphi$  and height  $l_s$ ; if the joints in the two ends of a strut component differs in diameter, i.e.,  $\varphi_{j1} \neq \varphi_{j2}$ , the strut is then a circular truncated cone instead. Next, the fillet geometry is defined as a cone wrapping around the joint. The joint was enlarged by a multiply factor  $f$  denoted as enlarge factor, and generate the transition cone between the joint and the strut with a bottom diameter of  $f\varphi_j$  and a height of  $h$  that is defined by a coefficient  $\mu$  as:

$$h = \mu f l_0 \quad (4)$$

where  $l_0$  is the length of the shortest strut as a reference.  $\mu$  is the height coefficient to make sure the cone provides a practical enhancement, which is fixed as 0.125 in this work. Considering the complexity of the overall CMMs structure and the variety of situations in which the struts intersect at a joint, the fully-defined cone-shape fillet can be well adapted in the proposed design method. The introduction of joint enhancement is supported by the analysis based on rigidity theory, which is utilized to study the stability of mechanical trusses by reducing complex networks (such as lattices) to nodes constrained by rods [60,61]. In this work, the increasement in the flexibility of CMMs by the fillet enhanced-joints was elucidated in Appendix A.2.

**2.2.2. Bio-inspired helix design.** Considering the feature of uniaxial crashworthiness test, the metamaterial macrostructures were built layer by layer along the axial direction ( $z$ -direction). By laying the design space of each layer in a certain direction to form a rotation angle with adjacent layers, a helix design follows the natural character of chirality [62]. And the application on energy absorption can also be inspired from the Bouligand structure [52,53]. In this way, a helix CMM can be generated by setting an angle  $\Delta\theta_i$  between layer  $i$  and layer  $i + 1$ , as shown in Fig. 3(c). It is important to note that this contributes to the flexibility of the aperiodic framework from a multi-scale perspective: regulating the shape of the design space at the macro-structure and defining the unit-cell geometry at the micro-scale.

**2.2.3. Bi-directional gradient design.** The graded geometry in this multi-scale design was further introduced. Herein, a bi-directional gradient CMMs design was presented by varying the unit-cell size along both radial and axial directions. Specifically, the design is controlled by the gradient coefficients of these two directions, denoted as  $\zeta_r$  and  $\zeta_a$  respectively. As a fundamental investigation, the overall size of CMMs samples is set as  $L_x \times L_y \times H = L \times L \times H$  with side length  $L$  and height  $H$ . Thus, the size of unit cell is defined by given the number  $N_x \times N_y \times N_z$  as

$$a_x \times a_y \times a_z = \frac{L}{N_x} \times \frac{L}{N_y} \times \frac{H}{N_z} = l_0 \times l_0 \times h_0 \quad (5)$$

A reference size was set for the unit cell in the first layer bottom-up along axial direction according to Eq. (5). Then, the side lengths and heights of unit cells along the radial and axial directions can be determined by geometric series with the gradient coefficients  $\zeta_r$  and  $\zeta_a$  as their respective common ratio, expressed as

$$\sum_{i=0}^{N_x-1} \zeta_r^i = \frac{1 - \zeta_r^{N_x}}{1 - \zeta_r} = \frac{L}{l_0} \quad (6)$$

$$\sum_{i=0}^{N_z-1} \zeta_a^i = \frac{1 - \zeta_a^{N_x}}{1 - \zeta_a} = \frac{H}{h_0} \quad (7)$$

Based on Eq. (6) and Eq. (7), the size of each vertical and diagonal strut can be derived by locating the position of each joint. Generally, a positive  $\zeta_r < 1$  guarantees a tower-shaped macrostructure of CMMs and  $0 < \zeta_a < 1$  means that the layer height decreases from bottom to top. In this work, gradient design with  $\zeta_r = 0.930$ ,  $\zeta_a = 0.928$  was applied to the CMMs with and without helix, as illustrated in Fig. 4. The

rotation angle between layers is set uniform as  $\Delta\theta = 4.5^\circ$ . The structures that only have radial gradient were also generated. And it is noted that the gradient coefficients can be negative to make reverse geometries. Here, chiral mechanical metamaterials with negative axial gradient  $\zeta_a = -0.928$ , which have a “sharp” tower shape at top layers, are demonstrated for comparison. The effect of bi-directional gradient geometry on energy absorption will be later elucidated. Last but not least, the proposed CMMs can have local adjustment by making struts slender, as shown in Fig. 3(c). Through the reduced diameter of joint as  $\varphi'_{jv} = f_{jv} \cdot \varphi_{jv}$ , the rod connecting the joint can be consequently slimmed in its diameter.  $f_{jv}$  is defined as slender factor.

At this point, a parametric design with chiral configuration, which is general to lattice-based mechanical metamaterials, has been achieved. The full description of CMMs including the basic parameters of unit-cell, macrostructure, the scalable assembly criteria, and the factors or coefficients controlling the geometry is listed in Table 1.

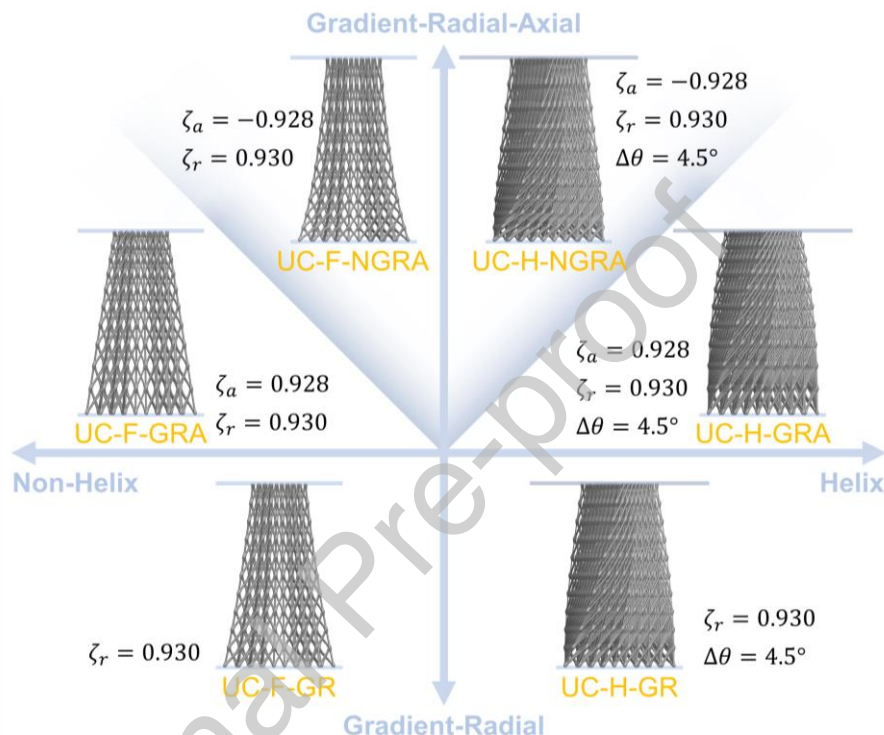


**Fig. 4. Bi-directional gradient design of chiral mechanical metamaterials.** The CMMs with unified chiral (UC) configurations are presented. Both the helix design (UC-H) and non-helix one (only with fillet-enhanced joint, UC-F) are adapted by radial-axial graded geometry (-GRA) or radial gradient (-GR). Also, negative axial gradient is applied in this bi-directional gradient design (-NGRA).

**Table 1.** Parameterization of the proposed chiral mechanical metamaterials design framework.

Geometric Parameters	Description
$L_x \times L_y \times H$	Overall sizes of the CMMs samples.
$N_x \times N_y \times N_z$	Numbers of spaces separated by the joints in three directions.
$f \cdot [\varphi_{J_{i,j,k}}]$	Diameters of joints $\varphi_J$ amplified by enlarge factor $f$ .
$A(\mathbf{r}_i, \mathbf{e}_i, h^k)$	Assembly criteria to determine the chiral configuration.
$h$	Height of the joint-enhanced cone.
$f_{jv}$	Slender factor to reduce the diameter of the vertical strut.
$\Delta\theta_i$	Helix angle between layers.
$\zeta_a, \zeta_r$	Gradient coefficients for axial and radial directions.

### 2.3. Settings of medium-strain-rate impact

**2.3.1. Experiment.** In this work, uniaxial dynamic compression tests were conducted to obtain the mechanical behaviors of the proposed CMMs. Using a high-speed mechanical test machine, Instron VHS 160/100-20, the 3D-printed CMMs samples were crushed along their axial direction by a vertical punch with given velocity, as shown in Fig. 5. The rotation of the punch is friction-free, releasing the corresponding twist DOF.

Considering the constraints of SLM and experiment, each CMMs sample was attached by a bottom panel and a top panel along the axial direction ( $z$ -direction) to guarantee a uniform boundary condition. The overall size is set as  $L \times L \times H = 60 \text{ mm} \times 60 \text{ mm} \times 100 \text{ mm}$  (for helix sample it is the design space before rotation), with the number of joints as  $(N_x + 1) \times (N_y + 1) \times (N_z + 1) = 10 \times 10 \times 11$ . Referring to Eq. (5), the initial unit-cell size can be derived as  $a_x \times a_y \times a_z = l_0 \times l_0 \times h_0 = 6 \text{ mm} \times 6 \text{ mm} \times 10 \text{ mm}$ . The joint diameter and the enlarge factor are defined as unified everywhere to generate struts with unified diameter, i.e.,  $\varphi_{j1} = \varphi_{j2} = d$ . For different types of CMMs samples 3D printed in this work,  $d$  was varied from 0.6 mm to 2.0 mm, and  $f$  from 1.0 to 2.0. Meanwhile, the bottom and top panels are of size 70 mm  $\times$  70 mm  $\times$  2 mm.

With the samples set and manufactured, the boundary conditions were then determined to ensure that the bottom panel was fixed, and the top panel was imposed by an axial impact from the punch with a constant velocity of 5 m/s (18 km/h) and a displacement of 75 mm. Thus, the strain rate can be calculated as  $\dot{\varepsilon} = \varepsilon_{zz}/\Delta t = 50 \text{ s}^{-1}$ , leading a medium-strain-rate impact case for CMMs to absorb energy.

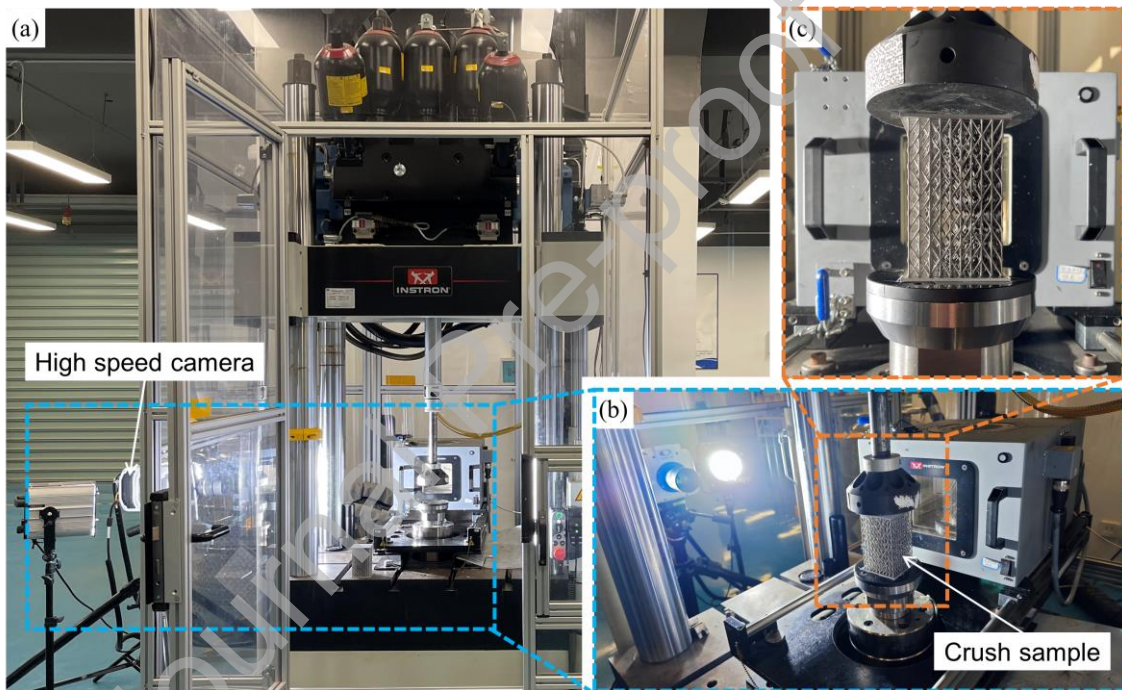


**Fig. 5. The experiment system to test the medium-strain-rate dynamic compression.** (a) The high-speed mechanical test machine Instron VHS 160/100-20 with a high-speed camera. (b) The proposed CMMs samples are placed vertically along the axial direction. (c) The punch of the machine can rotate freely along the axial direction.

**2.3.2. Finite element analysis.** Another aspect of the proposed CMMs design framework is the modeling method for finite element analysis (FEA), as illustrated in Fig. 6. In this study, FEA is conducted using ABAQUS Explicit. The modeling procedure follows: Firstly, the material properties of SLM stainless steel 316L are inputted. Considering the large deformation and high strain rate of the impact process, Johnson-Cook (J-C) constitutive model was used to characterize the mechanical behavior of 316L. Neglecting temperature effects, the detailed constants of the applied J-C plasticity model and failure model are presented in Appendix A. Secondly, the boundary conditions are consistent with that of the experiment, where the fixed bottom panel and the free top panel are constrained as rigid. And the top panel interacts with a rigid wall that drops along  $z$ -direction using a hard contact, as shown in Fig. 6(a). The rigid wall is large enough to cover the collision area of CMMs. Thirdly, two loading cases were set for energy-absorbing performance of CMMs. Defined as case 1, the rigid wall compresses the samples by  $s = 80 \text{ mm}$  with a constant velocity of 5 m/s, corresponding to the experimental conditions. While in case 2, the rigid wall is endowed with a mass and moment of inertia of 150 kg and drops at an initial velocity of 5 m/s.

Fourthly, the FEA model is meshed from the CAD model. To establish a FEA model of high fidelity, traditional finite element modeling method may discretize the CAD model directly by solid elements, which is unacceptable in computational efficiency considering the fact that the proposed CMMs samples meshed by tetrahedron elements can exceed the computing power of our computers (over 20 million elements) and has a bad meshing quality of the joints. Therefore, an efficient parameterized meshing method was proposed as illustrated in Fig. 6(b) and (c). Specifically, the idea was built on the concept that, each strut component along with the enhanced joints at its two ends is meshed respectively. After that, the struts are assembled by constraints in accordance to the pre-defined connection relationships in Fig. 3(b). Approximating the circular cross-section of strut to an octagon, all struts can be regularly meshed along their perspective axial direction using the C3D6 wedge elements in ABAQUS. The approximate global size of element is set as 0.5mm after convergence analysis (Refer to Appendix A.4.). To do this, the nodes within a cross-section are defined in a local coordinate and then mapped into the global coordinate based on the position and orientation of the strut, as shown in Fig. 6(c). (Refer to Appendix A.5. for more details). With each strut component discretized, the multiple point constraint (MPC) was applied at the central reference points to assemble the struts to joints, as demonstrated in Fig. 6(b). Reducing the element number to 3.5 – 4 million, the meshing method is efficient via replacing the heavy manual operation in modeling by automatic parametrical process.

Finally, with the material properties set and meshing method applied, the uniaxial crash simulation can be conducted. In the step of ABAQUS, the target time increment was set as  $1 \times 10^{-6}$ . In case 1, the compressive response of CMMs can be investigated, and through the second case, the displacements under the same initial kinetic energy can be compared among different CMMs. The results were post-processed as force-displacement curves and force-time curves by extracting the forces and displacements of the top panels. The uniaxial strain can be easily converted from the displacement as  $\varepsilon_{zz} = s/H$ . And the energy absorption (EA) can be calculated as:

$$EA = \int_0^{s_{ple}} F ds [kJ] \quad (8)$$

where  $s_{ple}$  is the displacement at the end of the yield plateau of CMMs and corresponds to the axial strain at densification as  $\varepsilon_d = s_{ple}/H$ . The plateau end  $s_{ple}$  is defined by the maximum deformation efficiency  $f_{max}$  which is expressed as:

$$f_{max} = \max \left( \frac{\int_0^s F(s) ds}{F_{max}} \middle|_{s=s_i} \right) = \frac{\int_0^s F(s) ds}{F_{max}} \Bigg|_{s=l_{max}} \quad (9)$$

where  $s_{ple} = l_{max}$ . The specific energy absorption (SEA) can be thus derived as:

$$SEA = \frac{EA}{M} = \frac{\int_0^{s_{ple}} F ds}{V \cdot \rho_s \cdot \rho^*/\rho_s} [kJ/kg] \quad (10)$$

where  $\rho_s = 7.98 \text{ g/cm}^3$ . And  $\rho^*/\rho_s$  stands for the relative density calculated as:

$$\frac{\rho^*}{\rho_s} = \frac{V_m}{V_s} = \frac{V_{in} + V_{sf}/2 + V_{sl}/4}{L^2 H} \times 100\% \quad (11)$$

Here,  $V_{in}$ ,  $V_{sf}$ , and  $V_{sl}$  correspond to the volumes occupied by the rods inside the CMMs structure, on the side faces, and at the side lines, respectively.

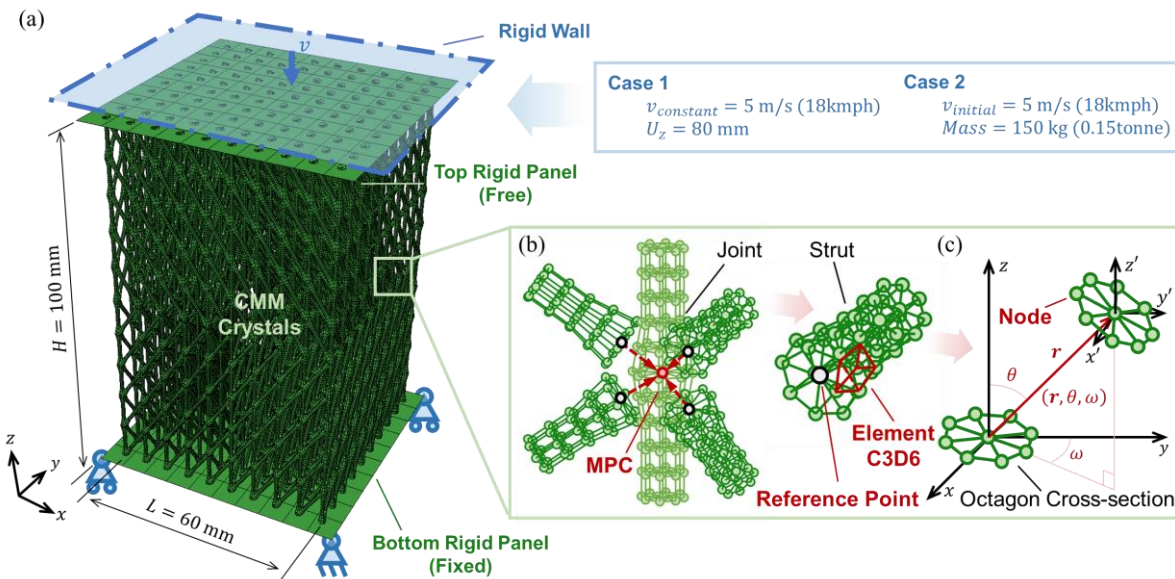


**Fig. 6. Finite element analysis of the CMMs samples.** (a) Boundary conditions of the dynamic compression. (b) The discretization of struts. After the strut is meshed by C3D6 elements, the reference point couples the nodes at the end of the strut. Then the strut is constrained to the joint by multiple point constraint (MPC). (c) Coordinate transformation of cross-section nodes from local coordinate to the global one.

### 3. Results and discussion

In this section the energy absorption capabilities of CMMs were shown. The chiral features of lattice-based metamaterials were first characterized, and then the mechanical behaviors of various configurations were demonstrated through a comprehensive comparative analysis. Following that, the deformation modes of the CMMs were investigated, illustrating the effectiveness of the aperiodic designs. The structure-property relationships were further elucidated. Finally, the energy-absorbing improvement by the proposed CMMs designs was discussed.

#### 3.1. Characterization of chirality

With geometric dimensions determined in Section 2.3, various types of the proposed CMMs with respect to representative chiral configurations have been generated by commercial software NX UG 12.0, as shown in Fig. 7. According to the ways the axial layers are arranged, the configurations are referred as unified chirality (UC), mirrored chirality, mixed chirality, and stochastic achiral respectively. The unified chirality has 10 right-handed layers, whereas the mirrored one has the upper 5 layers right-handed and the bottom 5 layers left-handed. And the mixed chirality is a more general configuration with more reverse changes of handedness between layers. Intuitively, it is necessary to describe the geometrical features of different configurations in order to distinguish different degrees of chirality. Herein, a chiral characterization method for the lattice-based CMMs was proposed.

First of all, indices are needed to guide the design. With uniaxial twist response, the CMMs crystal can be viewed as a combination of multiple  $z$ -directional layers, and the chirality of each layer can be tailored independently. Thus, the average handedness of each layer referring to Eq. (2) can be defined as:

$$c_{k,z} = \frac{1}{B_{k,z}} \sum sgn(\tilde{\mathbf{e}} \cdot \mathbf{r}_i \times \mathbf{e}_i) \quad (12)$$

where  $B_{k,z}$  is the number of the base chiral structures in the  $k$ -th layer. For the specific chiral structure in Fig. 7,  $B_{k,z}$  is calculated to be 180. And it can tell that  $c_{k,z} \in [-1, +1]$ . In this way, the chirality of the CMMs can be defined as:

$$\mathbf{C}_Z = [c_{k,z}]_{1 \times N_z} \quad (13)$$

which is referred to as Assembly Matrix to define the chiral configurations of each layer.

Referring to Eq. (13), the assembly matrix has  $N_z$  numbers of components  $c_{k,z}$ , which indicates the degrees of chirality corresponding to the axial layers. Clearly, the chiral configuration of the axial layer is in one-to-one correspondence with  $c_{k,z}$  when  $c_{k,z}$  obtains an extremum, i.e.,  $c_{k,z} = \pm 1$ . As a result,  $\mathbf{C}_Z = [+1, +1, +1, +1, +1, +1, +1, +1, +1, +1]$  for the presented unified chirality (right-handedness). And the assembly matrix of the mirrored chirality and the mixed chirality can be written as

$[-1, -1, -1, -1, -1, +1, +1, +1, +1, +1]$  and  $[+1, +1, +1, -1, -1, +1, -1, -1, +1]$  respectively. It is noted that the mixed chirality can have a large variety of configurations through the permutations of axial layers, one of which is the mirrored chirality. However, it is not the case when the handedness average index ( $c_{k,Z}$ ) is in between. Different combinations of the diagonal struts can have the same  $c_{k,Z}$ . With  $\mathbf{C}_Z = [+1.1, -4.4, +5.6, +2.2, -6.7, +2.2, +6.7, +2.2, +14, -23]$ , Fig. 7(d) shows one stochastic generation which enables an achiral CMMs by ensuring the overall degrees of handedness equal to zero, i.e.,  $\sum c_{k,Z} = 0$ . It can be indicated that, individual layer may rotate in response to the compressive displacement according to the inherent handedness, but the macrostructure is irrotational between the upper and lower boundaries as long as  $\sum c_{k,Z} = 0$ . Therefore, the achiral CMMs along with the mirrored and mixed CMMs exhibit no overall twist DOF, the result of which will be presented and discussed in Section 3.2.

Next, after the chiral configurations are determined by the assembly matrix, evaluations need carrying out to characterize the chirality from the geometrical features of diagonal struts. Because only the sign of the calculated screw is used in the assembly criteria as in Eq. (2), the Z-shaped chiral unit cell of different sizes can have the same  $\mathbf{C}_Z$ , which cannot explain the impact of each basic geometric change on the overall macrostructure of CMMs. Thus, inspired by the orientation tensors in mean-field homogenization (MFH) of composite materials [63], the chiral index was introduced to measure the overall chirality (OC) of lattice-based metamaterial crystals generated by the proposed design method.

Specifically, based on the description in Section 2.1, suppose  $\mathbf{p}_i = \hat{\mathbf{r}}_i \times \mathbf{e}_i$  is the chiral vector of arbitrary inclined strut in unit cells where  $\hat{\mathbf{r}}_i$  is the projective vector of  $\mathbf{r}_i$  in the plane perpendicular to the rotation center  $\tilde{\mathbf{e}}$ . With various chiral unit cells distributed in the CMMs crystal,  $\mathbf{p}_i$  forms an orientation-dependent field inside the metamaterial, denoted as  $\mu(\mathbf{p}_i)$ . In this way, each chiral microstructure has an oriented description in Cartesian coordinate. Its orientation average is the integral over all orientations, weighted by the orientation distribution function  $\Psi(\mathbf{p}_i)$ :

$$\langle \mu(\mathbf{p}_i) \rangle_\Psi = \oint \mu(\mathbf{p}_i) \Psi(\mathbf{p}_i) d\mathbf{p}_i \quad (14)$$

Thus, the index is defined as the following orientation average:

$$\alpha_Z \equiv \langle \mathbf{p}_i \otimes \mathbf{p}_i \rangle_\Psi \quad (15)$$

It can be derived that  $\alpha_Z$  is a symmetric second-rank tensor and measures the overall chirality of CMMs, namely OC. With chiral configuration fixed, OC varies in accordance to the geometric parameters of struts. And on the other hand, OC is influenced by the arrangement of chiral base structures given their sizes. The values of OC of the four configurations in Fig. 7 are listed in Table 2.

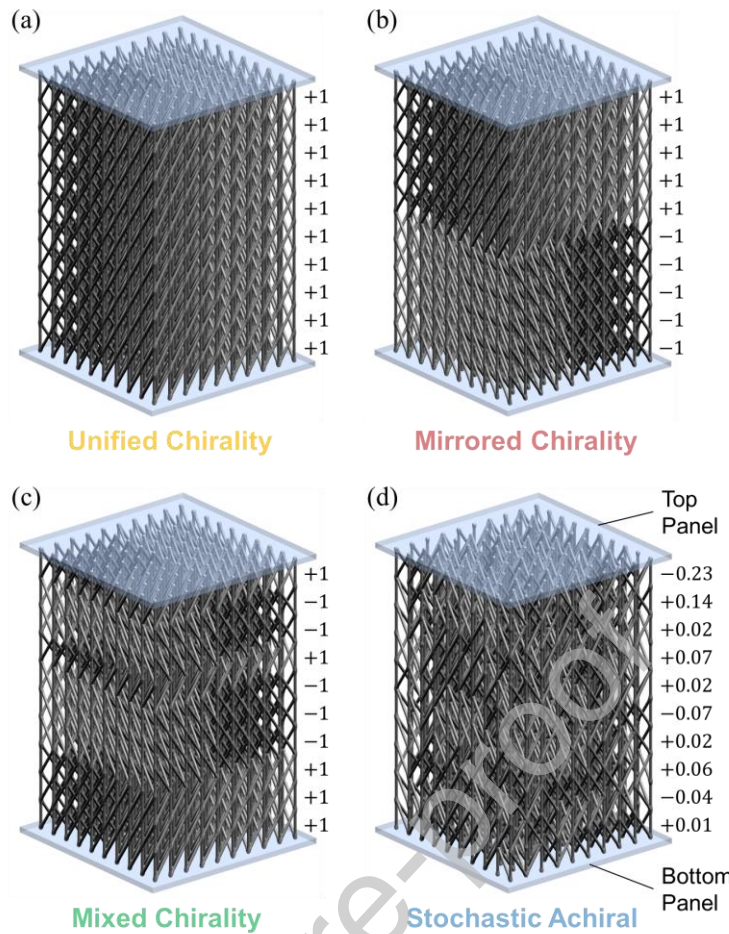


**Fig. 7.** The representative configurations of the proposed CMMs. (a) Unified chirality which has unified right-handedness everywhere. (b) Mirrored chirality which is divided into two from the middle with opposite handedness. (c) Mixed chirality with the handedness of the axial layers defined independently. (d) One of the achiral configurations generated stochastically with the handedness of each Z-shaped base structure defined independently. The real numbers labeled on the right side of each subgraph represent the  $c_{k,Z}$  of each layer.

It can be found that, regardless of the handedness (direction of rotation), the unified, mirrored, and mixed chirality share the same OC as expected due to the same basic geometric settings of samples (see Section 2.3), the same ISA  $\tilde{e}$ , and the extremum value of  $c_{k,Z}$  for each axial layer. Also, OC is reduced to a diagonal matrix  $\alpha_z(\alpha_1, \alpha_2, \alpha_3)$  with  $\alpha_1 = \alpha_2$  due to the equivalent features in  $x$  and  $y$  directions (as radial directions for CMMs). Thus, it can have

$$\alpha_z = \begin{bmatrix} (1 - \alpha_3)/2 & & \\ & (1 - \alpha_3)/2 & \\ & & \alpha_3 \end{bmatrix} \equiv f(\alpha_3) \quad (16)$$

for all the CMMs designs of the proposed framework. As for the stochastic achiral CMMs, its OC is slightly deviated, but is still considered approximately the same as that of the other configurations for the same strut dimensions defined. The deviation and the consistency of chirality between layers (CC) were further characterized in Appendix A. Consequently, the characterization of the chiral geometry features of the proposed lattice-based CMMs is established. As demonstrated in Fig. 8, the design variants of the unified chiral configuration under the presented framework indicate the generality of the characterization.

**Table 2.** Characterization of the chirality of the proposed CMMs.

Configurations	Overall chirality (OC), $\alpha_z$
----------------	------------------------------------

Unified	$\begin{bmatrix} 0.4105 & & \\ & 0.4105 & \\ & & 0.1789 \end{bmatrix}$
Mirrored	$\begin{bmatrix} 0.4105 & & \\ & 0.4105 & \\ & & 0.1789 \end{bmatrix}$
Mixed	$\begin{bmatrix} 0.4105 & & \\ & 0.4105 & \\ & & 0.1789 \end{bmatrix}$
Achiral	$\begin{bmatrix} 0.4127 & 0.0028 & 0.0065 \\ 0.0028 & 0.4096 & 0.0035 \\ 0.0065 & 0.0035 & 0.1777 \end{bmatrix}$

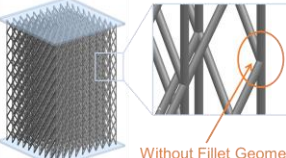
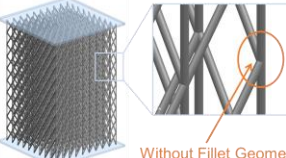
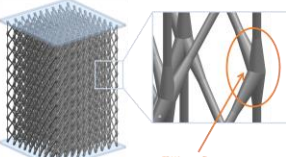
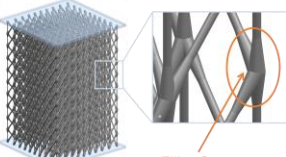
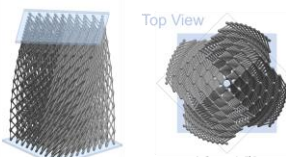
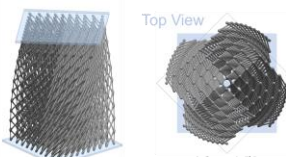
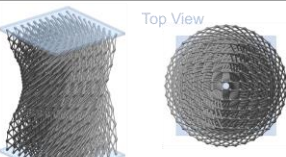
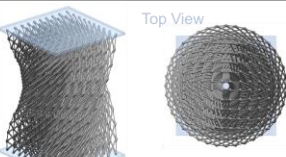
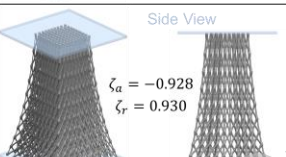
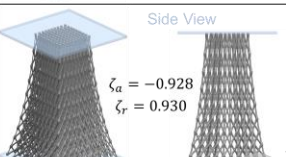
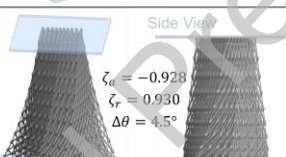
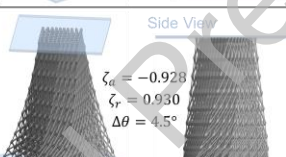
Referring to Eq. (14) to Eq. (16), the three components of  $\alpha_z$  represent the orientation distribution of the chiral vector. In conjunction with its variation in Fig. 8, it can be concluded that, a larger pitch makes diagonal struts more upright, and thus causing a smaller  $\alpha_3$ , which elucidates the programmable chiral characteristics of the CMMs.

### 3.2. Crush behaviors of chiral mechanical metamaterials

With various CMMs configurations that the proposed design framework can generate, the crush deformation patterns and energy-absorbing capabilities of these designs were presented and discussed in this section.

**3.2.1. Dimension analysis of SLM samples.** Good manufacturing quality of the 3D-printing samples should be guaranteed. As shown in Fig. 9, dimensional analysis was conducted to validate the forming accuracy in size and shape of the printed samples. As shown from Fig. 9(a) to 9(d), the prepared unified, mirrored, mixed, and achiral samples were tested for compactness with penetrant, and the forming dimensions were measured with vernier calipers. The analysis of the geometrical features along z-direction was emphasized because the dimension in self-supported printing direction is more difficult to be guaranteed. Hereby the overall height  $H$ , the strut diameter  $d$ , and the panel thickness  $t$  of the fabricated samples were measured. As illustrated in Fig. 9(e), the dimensions were averaged by twenty different measured locations of the chiral configurations introduced in Section 2.3, and divided by their respective nominal sizes for a fair comparison, as  $H/\bar{H}$ ,  $d/\bar{d}$ , and  $t/\bar{t}$ , where  $\bar{H} = 100$  mm,  $\bar{d} = 1$  mm, and  $\bar{t} = 2$  mm. The results show that the 3D-printed forming dimensions are generally larger than the nominal dimensions, with the relative errors of the strut diameter controlled within 5 % and even within 0.5 % for the overall height. This illustrates a reliable fabrication process of SLM CMMs for further experiments.

**3.2.2. Basic deformation mechanism of CMMs.** With the design and test approaches as explained in Section 2, basic understanding of the deformation mechanism can be formed via the compressive responses of the unified CMMs, as shown in Fig. 10. Under case 1 (constant velocity of 5 m/s), the force-displacement ( $F$ - $s$ ) curves of the unified configurations along with the in-situ deformation observation are extracted. The typical nonlinear compressive process of bending-dominated materials is reflected, where elastic deformation, plastic yield plateau, and densification occur sequentially. The unified CMMs with fillet (Fig. 7a) is referred to as UC in Fig 10(a). Under the dynamic compression, it exhibited a long and uniform plastic collapse after a high first peak forth  $F_{pk}$  which reached 70.37 kN. The collapse displacement reached over 75 mm until densification, corresponding to the uniaxial strain  $\varepsilon_d = 76.7\%$ .

		$d/l$ (%)	$\rho^*/\rho_s$ (%)
Original	 Without Fillet Geometry	4.99 8.32 12.48	2.43 5.57 11.42
		$\alpha_Z = \begin{bmatrix} 0.4105 & & \\ & 0.4105 & \\ & & 0.1789 \end{bmatrix}$	
Fillet		$d/l$ (%)	$\rho^*/\rho_s$ (%)
	 Fillet Geometry	4.99 8.32 12.48	3.64 8.39 16.95
		$\alpha_Z = \begin{bmatrix} 0.4083 & & \\ & 0.4083 & \\ & & 0.1834 \end{bmatrix}$	
Fillet-Helix		$d/l$ (%)	$\rho^*/\rho_s$ (%)
	 Top View $\Delta\theta = 4.5^\circ$	4.99 8.32 12.48	3.83 8.89 18.02
		$\alpha_Z = \begin{bmatrix} 0.3549 & & \\ & 0.3549 & \\ & & 0.2902 \end{bmatrix}$	
Gradient		$d/l$ (%)	$\rho^*/\rho_s$ (%)
	 Side View $\zeta_a = -0.928$ $\zeta_r = 0.930$	4.99 8.32 12.48	4.06 9.42 18.95
		$\alpha_Z = \begin{bmatrix} 0.3051 & & \\ & 0.3051 & \\ & & 0.3899 \end{bmatrix}$	
Gradient		$d/l$ (%)	$\rho^*/\rho_s$ (%)
	 Side View $\zeta_a = -0.928$ $\zeta_r = 0.930$ $\Delta\theta = 4.5^\circ$	4.99 8.32 12.48	3.38 7.70 16.23
		$\alpha_Z = \begin{bmatrix} 0.4395 & & \\ & 0.4395 & \\ & & 0.1209 \end{bmatrix}$	
Gradient		$d/l$ (%)	$\rho^*/\rho_s$ (%)
	 Side View $\zeta_a = -0.928$ $\zeta_r = 0.930$ $\Delta\theta = 4.5^\circ$	4.99 8.32 12.48	3.46 7.94 16.86
		$\alpha_Z = \begin{bmatrix} 0.4030 & & \\ & 0.4030 & \\ & & 0.1941 \end{bmatrix}$	

**Fig. 8. The design variants of the unified chiral mechanical metamaterials and the chiral characterization.**

Along with the original CMMs, the joint-enhanced design with fillet geometry, the fillet-helix design, and the gradient and helix-gradient design are generated with various strut diameters which are expressed as aspect ratio (diameter to length of the diagonal strut). The corresponding relative density is calculated by Eq. (11).

Excessive first peak force which indicates a large stiffness is not always a good thing for energy absorption processes. But it is unavoidable considering the reinforcing effect of the strain rate and the vertical struts that are straight in the direction of impact. To explain this, the vertical struts serve as the structural frame with stretching-dominated behavior while the diagonal ones form the chiral geometry with bending-dominated behavior. One way to improve this is to incline the vertical struts through helix design [62], which is discussed later. And another way is to make the vertical struts thinner based on the slender design introduced in Section 2.2, by which UC with the same diagonal struts but slimmer vertical struts was generated (denoted as UC-S). Specifically, the slender factor is uniformly set as  $f_{jv} = 0.6$ . Under the same boundary conditions, UC-S reduced  $F_{pk}$  and the average force at the yield plateau  $F_{pl}$  simultaneously, as presented in Fig. 10(a). Also, it delayed the densification to  $\varepsilon_d = 79.5\%$ . Calculating the corresponding EA and SEA according to Eq. (8) and Eq. (10), there is a respective 29.0 % and 25.0 % difference between UC and UC-S. By locally adjusting the geometry, the preliminary regulatory relationship between the structure and mechanical properties of the proposed CMMs is elucidated.

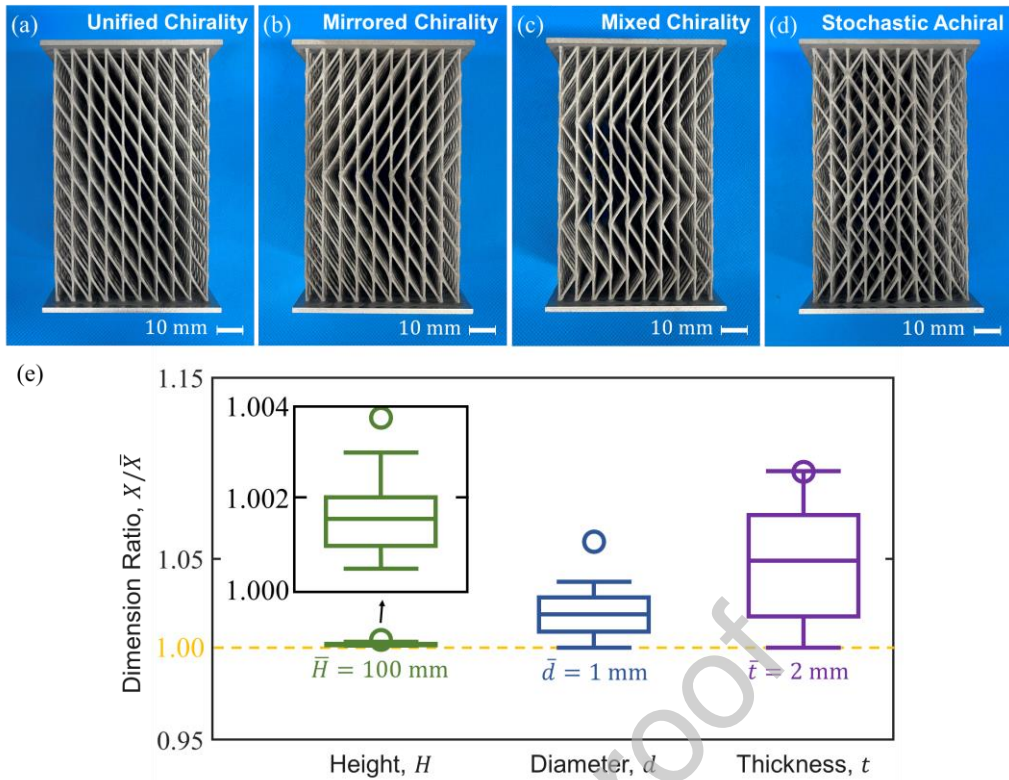


**Fig. 9. The manufactured CMMs samples and the dimensional analysis.** The side views of the SLM samples with (a) unified chirality, (b) mirrored chirality, (c) mixed chirality, and (d) achiral configurations. (e) Box plot illustrating dimensional analysis.  $X/\bar{X}$  in y-axis represents the ratio of the measured to the nominal sizes of overall height  $H$ , rod diameter  $d$ , and panel thickness  $t$  respectively.

Moreover, the material collapse process in Fig. 10(a) demonstrates the compression-torsion coupling of chiral metamaterials under large deformation. The diagonal strut of each Z-shaped chiral unit cell bends in the direction instructed by the corresponding instantaneous screw axis  $e_i$ , which accumulates into an overall deformation with a specific handedness given in design. With the plastic buckling of the vertical struts and the bending of the diagonal ones, the sample appeared an obvious shear zone along the diagonal direction, collapsing layer by layer from top to bottom and twisting concomitantly. Take a closer look at the deformation and failure modes of sample UC-S by Fig. 10(b) to 10(d), large twist angle is observed from the top view, and the vertical struts are folded in an S-shape. The S-shaped bending occurs close to the joints where the plastic hinge formation is most pronounced, which responds to the rigidity-theory-based assumptions made in the previous instant PRBM for joint-enhanced struts. A very small number of the slender vertical strut breaks were also observed, with the cracks occurring in the midsection with the thinnest rod diameter.

**3.2.3. Mechanical responses with respect to various configurations.** Besides the unified chiral mechanical metamaterials, the other proposed CMMs configurations have been tested for their dynamic responses. Fig. 11, Fig. 12, and Fig. 13, exhibit the mechanical behaviors of the mirrored, mixed, and achiral configurations, respectively. Consistent with UC in last subsection, the samples were all constructed using struts of diameter  $d = 1$  mm and tested in case 1. Generally, results from the  $F$ - $s$  curves in Fig. 11(c), Fig. 12(c), and Fig. 13(c) show that, all CMMs have an initial peak force of  $60 - 70$  kN at  $0.5\% - 1.0\%$  axial strain, and undergo a long and steady yield plateau until densification at around  $75\%$  axial strain. The side views of densified samples are shown in Fig. 11(b), Fig. 12(b), and Fig. 13(b). The axial strain is calculated as  $\varepsilon_{zz} = 100 \cdot s/H = s [\%]$ . And the average force during yield plateau is  $15 - 30$  kN. The SEA was calculated according to Eq. (10) and labelled in Fig. 11(c), Fig. 12(c), and Fig. 13(c), where the corresponding relative errors between the FEA and experimental results were also shown.

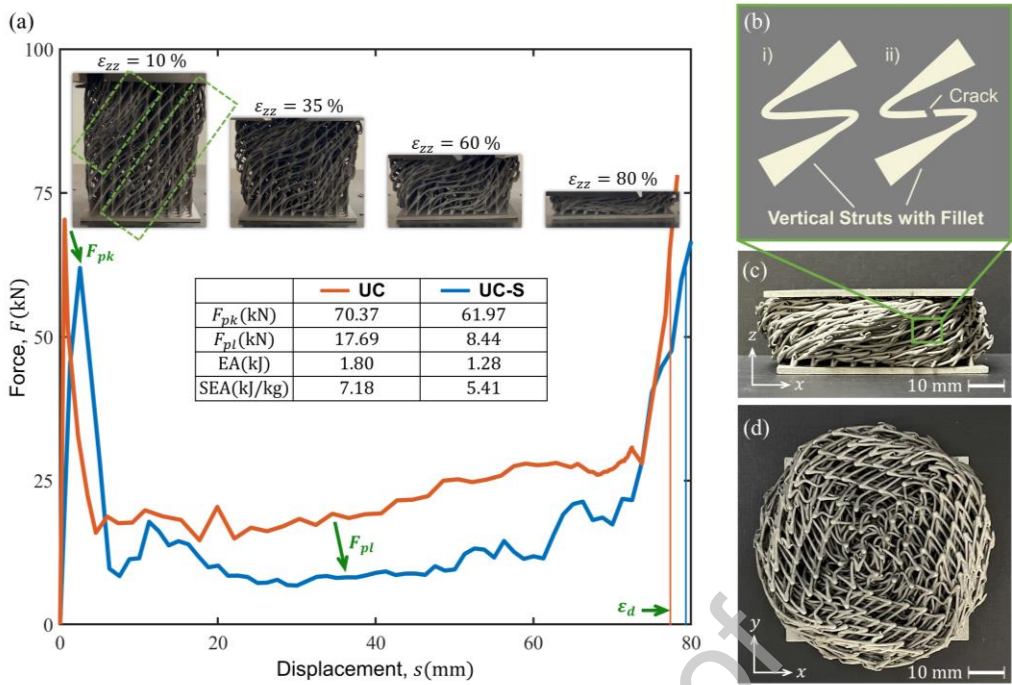


**Fig. 10. The mechanical responses of the proposed CMMs with unified chirality (UC).** Medium-strain-rate dynamic compression was conducted under case 1. (a) The force-displacement curves of UC and UC-S along with the in-situ observation at  $\varepsilon_{zz} = 10\%$ ,  $35\%$ ,  $60\%$ , and  $80\%$ . (b) The deformation and failure modes of vertical strut with fillet joints at its end. (c) Side view of UC-S sample and (d) the corresponding top view with the top panel removed.

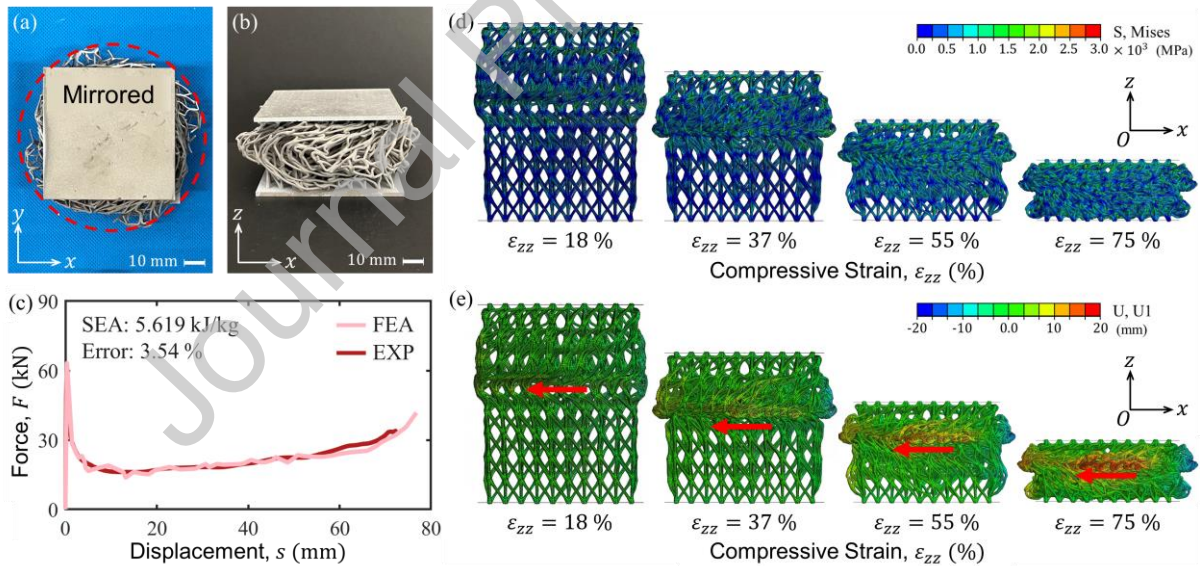


**Fig. 11. The mechanical responses of the proposed CMMs with mirrored chirality.** Medium-strain-rate dynamic compression was conducted under case 1. The (a) top view and (b) side view of densified sample show a nearly circular shape by rotation. (c) The force-displacement curves of experiment and FEA, along with (d) the Von-Mises stress contour and (e) the  $x$ -directional displacement field at  $\varepsilon_{zz} = 18\%$ ,  $37\%$ ,  $55\%$ , and  $75\%$ . The red arrows mark the rotation deformation of the layer.

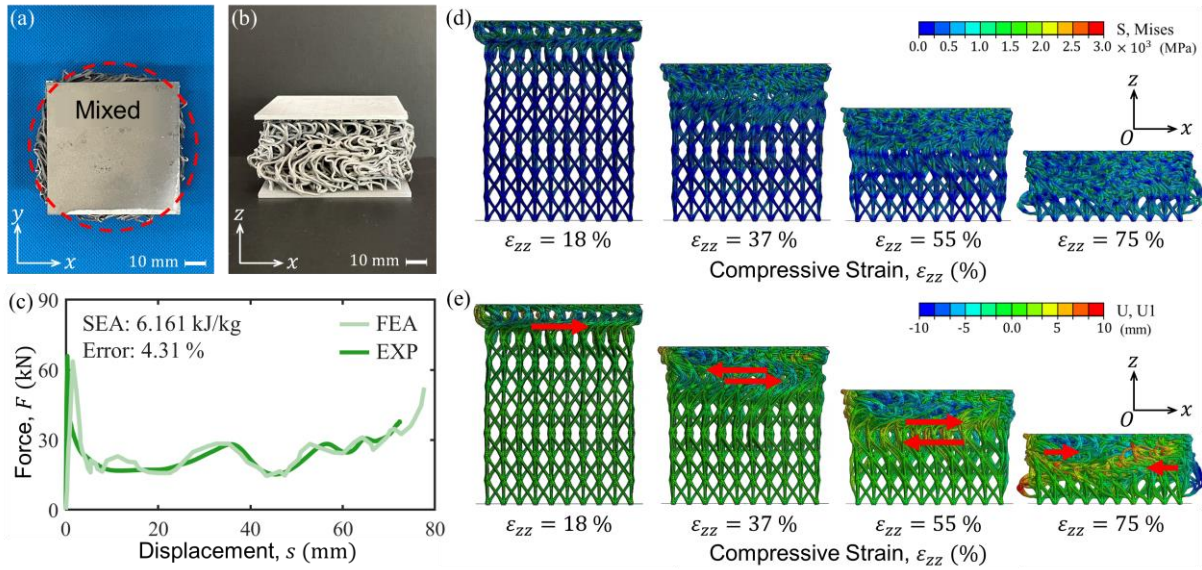


**Fig. 12. The mechanical responses of the proposed CMMs with mixed chirality.** Medium-strain-rate dynamic compression was conducted under case 1. The (a) top view and (b) side view of densified sample show a nearly circular shape by rotation. (c) The force-displacement curves of experiment and FEA, along with (d) the Von-Mises stress contour and (e) the  $x$ -directional displacement field at  $\varepsilon_{zz} = 18\%, 37\%, 55\%$ , and  $75\%$ . The red arrows mark the rotation deformation of the layer.

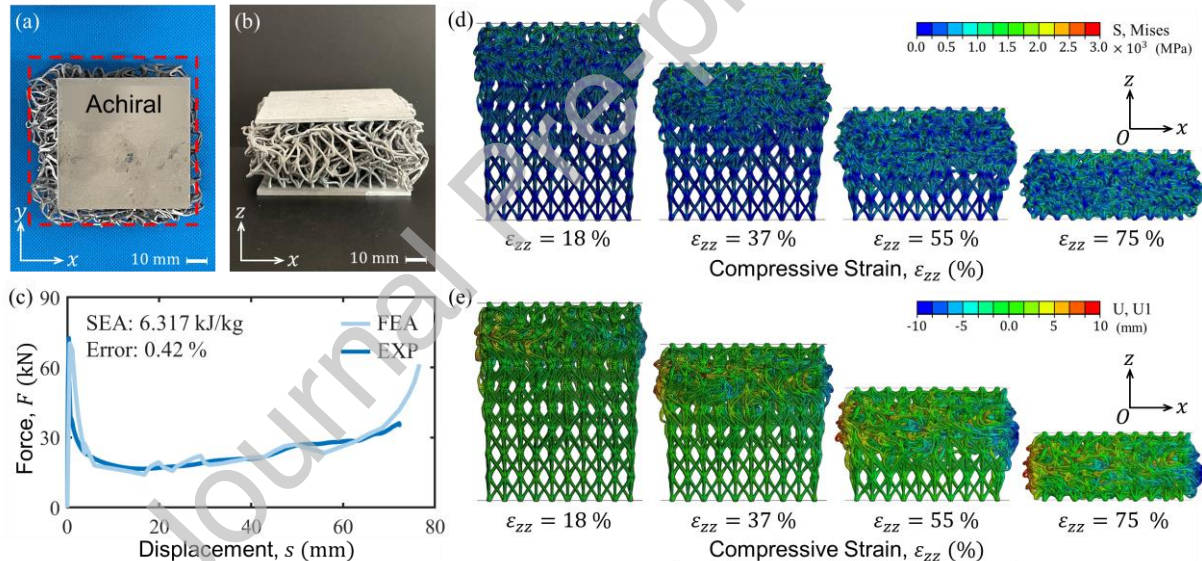


**Fig. 13. The mechanical responses of the proposed CMMs with achiral configuration.** Medium-strain-rate dynamic compression was conducted under case 1. The (a) top view and (b) side view of densified sample show a nearly square shape without rotation. (c) The force-displacement curves of experiment and FEA, along with (d) the Von-Mises stress contour and (e) the  $x$ -directional displacement field at  $\varepsilon_{zz} = 18\%, 37\%, 55\%$ , and  $75\%$ .

Combined with the results of the deformation process, the axial compressive deformation of the vertical struts is dominant at the beginning, leading to a steep increase in the overall structural high stiffness and compressive force, followed by a steep decrease when the struts undergo plastic buckling. Nevertheless, after the first peak force, the local deformation of the four configurations differs, which can be told from the shapes of the compressed samples in Fig. 11, Fig. 12, and Fig. 13. The material deformation under impact loading always occurs preferentially at the impacted end and passes downward layer by layer, and this law can be seen from the deformation process of the stochastic achiral configuration, as shown by the Von-Mises stress contour in Fig. 13(d) and displacement field in Fig. 13(e). In contrast, this is not the case for the mirrored chirality. Due to the chiral arrangement of the upper and lower layers with right- and left-handedness, respectively, the structure firstly flexes and bends in the junction layer with opposite rotational directions in the middle, as can be seen from Fig. 11(e). With medium strain rate, the deformation above and

below the junction layers is not strictly mirror symmetric, and the chiral layer close to the impact direction deforms and condenses first. As for the mixed chiral configuration, the interlayer chiral consistency is worse, i.e., there are more reverse of handedness between layers. As a result, more rotational deformation modes in the junction layers occur like that in the mirrored CMMs. And the order of priority is transmitted from top to bottom layer by layer along the impact. As shown in Fig. 12(e), the mixed chiral configuration is rotationally deformed under compression in multiple layers with opposite handedness, finally forming the deformation characteristic of "rotational folding". Interestingly, this can be evidenced by the compressed shape from the top views as shown in Fig. 11(a), Fig. 12(a), and Fig. 13(a), where the nearly circular densified samples of the mirrored and mixed chirality differ from the nearly square shape of the achiral configuration. And the circle of the mixed CMMs is smaller than that of the mirrored CMMs, meaning there exist more "rotational folding".

Corresponding to this deformation pattern is the "fluctuation" of the compressive force in the yield phase of the  $F$ - $s$  curve of the mixed chiral configuration in Fig. 12(c). When the uppermost junction layer undergoes rotational deformation, the rod structures gradually fail in bending and come into contact with each other, and the lower unflexed chiral layer continues to carry the force until the junction layer also rotates, resulting in a decrease in the compressive force, which is then carried by the lower unflexed structure. It is worth pointing out that, different with UC throughout the impact process, it can be observed that despite the occurrence of rotational deformation of the layers, the top and bottom panels of all three configurations do not rotate relative to each other, which is consistent with the proposed characterization of CMMs with a prescribed assembly matrix with  $\sum c_{k,z} = 0$ .

Furthermore, to better compare the mechanical properties and energy absorption performance of different designs under the proposed framework, the properties of the achiral lattices were used as benchmarks. As shown in Fig. 14, to achieve better generality, the joint-enhanced achiral CMMs with slender vertical struts ( $f_{jv} = 0.6$ ) were required by

$$\sum c_{k,z} = 0, |c_{k,z}| < 0.1 \quad (17)$$

Referred as Achiral-S, ten lattice-based samples were stochastically generated satisfying the requirement. Illustrated in Fig. 14(c) is the calibration of performance indicators.

### 3.3. Structure-property relationships under the design framework

**3.3.1. Effect of fillet design.** The effectiveness of the proposed joint-enhanced method is demonstrated in this subsection as shown in Fig. 15. With representative left and right handedness arranged symmetrically along compressive direction, the mirrored configuration was selected for demonstration. Firstly, the energy absorption with respect to the strut diameter was tested utilizing the  $F$ - $s$  curves of the mirrored CMMs under case 1. Obviously in Fig. 15(a), CMMs with the thicker struts has the less pronounced  $F_{pk}$  and the larger  $F_{pl}$ , accompanied by an earlier densification stage. By investigating the corresponding EA, as shown in Fig. 15(b), it can be concluded that the larger the diameter, the higher the amount of energy absorption. Not only that, it presents a positive proportional correlation between the absorbed energy and the third power of the strut diameter.

Furthermore, the influence of the reinforcement by different fillet joints on the compressive behavior was investigate. Set under case 2 where the total kinetic energy of a rigid wall is  $Mass \cdot v_{initial}^2 / 2 = 1.875$  kJ, the corresponding  $F$ - $s$  and  $F$ - $t$  curves of the mirrored CMMs are shown in Fig. 15(c) and 15(d). The diameter of enhanced joint is defined as  $f\varphi_j$  as mentioned in subsection 2.2. Thus, the mirrored CMMs with different enlarge factor  $f = 2.0$ ,  $f = 1.5$ , and  $f = 1.0$  were generated, where the joints keep original without fillet geometry by setting  $f = 1$ .

From the results, it can be observed that CMMs with enhanced joints have a relative smaller collapse displacement and a smaller response time. The total kinetic energy was absorbed by the mirrored CMMs with  $f = 2.0$  at a displacement of 50mm, whereas the other two did not completely prevent the movement of the rigid wall within 30ms. It can be concluded that the greater the joint reinforcement, the greater the yield compression force, and the smaller the collapse displacement and corresponding response time. Thanks to the fillet geometry, in the dynamic compressive mechanical behavior, the stress concentration at the joints of CMMs is not significant, and the failure of the struts is no longer concentrated at the joints at the two ends, greatly improving the impact toughness and stability of the structure.

**3.3.2. Effect of helix design.** As introduced in Section 2.2, the helix design of CMMs is inspired by the bionics. This also becomes a means of reducing the stiffness of the vertical rod at impact. In Fig. 16, the properties of various CMMs designs with respect to the strut diameter were compared, which elucidates the effect of helix. Specifically, the unified chirality is used to generate the variants of its original design, and

compressed under case 1. The helix angles were set  $9.0^\circ$  and  $4.5^\circ$  considering their special geometrical features, as shown in Fig. 8. For  $\Delta\theta = 9.0^\circ$ , the 10-layer CMMs can have a total  $90^\circ$  angle offset between the top and bottom panels, which also aligns the edges of the two panels. It can tell that the panels will be aligned in edges for every “aligned angle”, i.e.,  $\Delta\theta = 9.0^\circ \times n$ . And within an overall twist range from zero to  $90^\circ$ ,  $\Delta\theta$  that exceeds  $9.0^\circ$  is not considered because of the SLM manufacturability. As for  $\Delta\theta = 4.5^\circ$ , it's half of the “aligned angle”, which is also representative for this helix design research. In Fig. 16, UC, UC-F, and UC-H represent the unified CMMs without fillet, with fillet, and with fillet and helix design, respectively. Key indicators of CMMs under dynamic compression are measured, including energy absorption EA, specific energy absorption SEA, the first peak force  $F_{pk}$ , average plateau force  $F_{pl}$ , densification strain  $\varepsilon_d$ , compressive modulus  $E_c$ , specific compressive modulus  $e_c = E_c/M$ , twisting angle at densification  $\theta_z$ , and twisting angle per axial strain at densification  $\theta_z/\varepsilon_d$ .

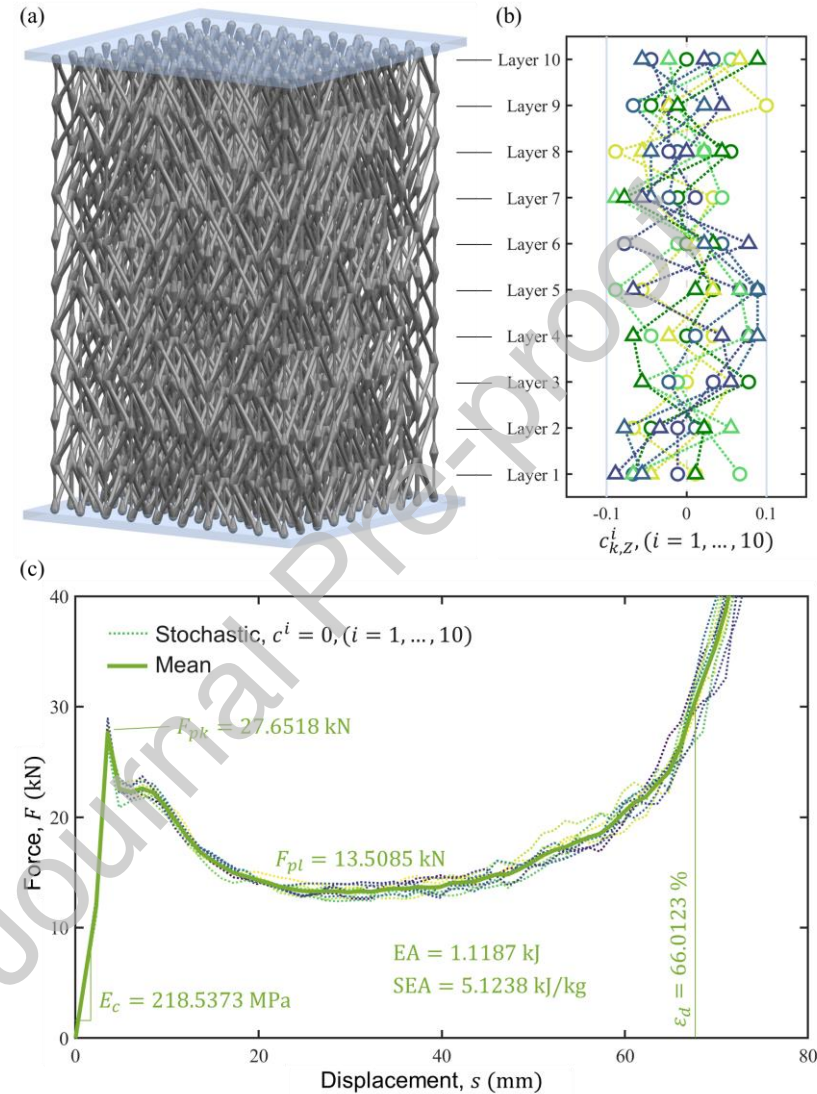


**Fig. 14. Mechanical properties of Achiral-S as benchmarks.** (a) Geometry model of one of the ten stochastically generated lattices. (b) The corresponding assembly matrix components satisfying Eq. (17). (c) The  $F$ - $s$  curves of Achiral-S.

The results show how the helix design differs from others. First, UC-H has lower compressive modulus and specific compressive modulus, which corresponds to the lower force  $F_{pk}$  and  $F_{pl}$ , as shown in Fig. 16(b) and (c). This proves that, with the vertical struts attribute to the large initial peak load, the inclination of the struts to a certain angle is effective to tailor the compressive behavior of CMMs with lower first peak force. However, the energy-absorbing properties of the helix CMMs were also reduced, as shown in Fig. 16(a). The reason for this is, on the one hand, the lower yield plateau force and, on the other hand, the smaller densification strain which implies an earlier end of energy absorption [25,64]. As seen in Fig. 16(b), the densification strain becomes smaller with increasing rod diameter for all CMMs designs, but the decay of

UC-H is more accelerated. Second, twisting angle at densification  $\theta_z$  shown in Fig. 16(d) indicates the upper limit of the rotational deformation that the lattice can achieve when absorbing energy. As the strut diameter becomes thicker, the  $\theta_z$  of UC and UC-F increases because the material tends to collapse in axial buckling rather than bending deformation when the rod is very thin. However, the twisting angle of UC-H becomes smaller due to the earlier contact behavior between the struts when  $d$  is large. The  $\theta_z$  along with  $\theta_z/\varepsilon_d$  of UC-F and UC-H are similar at small  $d$  and then diverge as the diameter increases. This also explains the smaller amount of energy absorption by showing that UC-H has less rotational deformation during compression. Next, Fig. 16(a) shows a consistent pattern of monotonically decreasing specific energy absorption with diameter, which indicates that as the strut diameter becomes thicker (corresponding to the aspect ratio  $d/l$ ), it is difficult to fully utilize the deformation of the material everywhere to absorb energy. The lattice-based structure always needs to find a balance between the material utilization and the total energy absorption. Finally, it can be concluded from the performance of UC-H with  $\Delta\theta = 4.5^\circ$  and  $\Delta\theta = 9.0^\circ$  that, the greater the degree of helical torsion of the CMMs macrostructure, the more pronounced the above pattern of change brought about by the helix design. This also implies that the appropriate parameter levels should be chosen to achieve the corresponding design target. Taken together, UC-F has the best performance in terms of energy absorption at the current operating conditions.

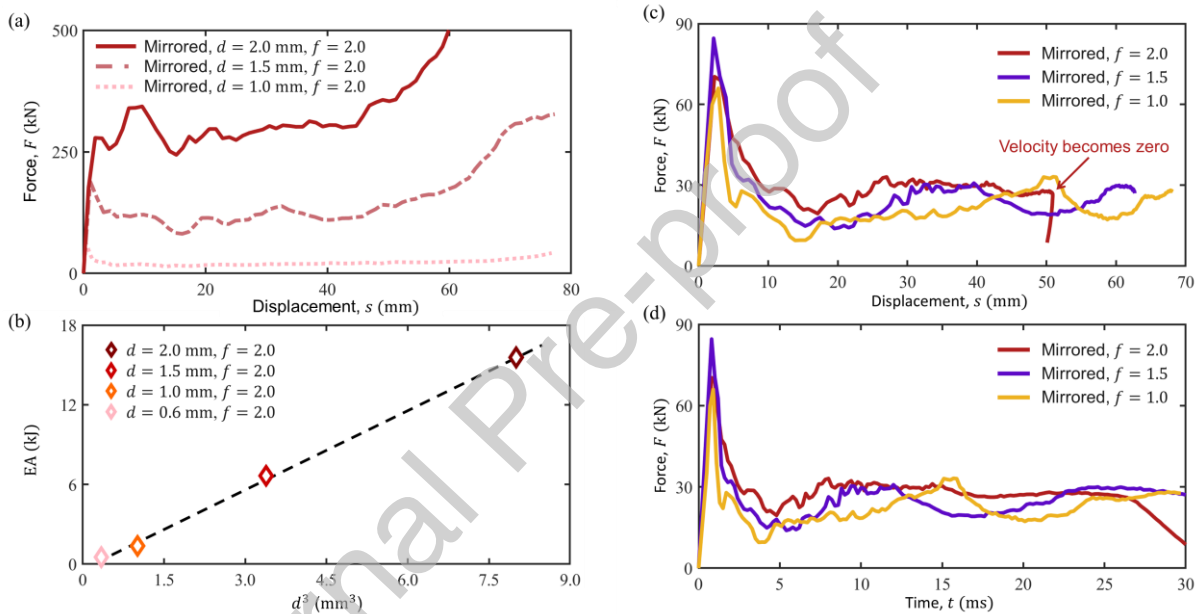


**Fig. 15. The effect of fillet design and strut diameter.** (a)  $F$ - $s$  curves of the mirrored CMMs with different strut diameters  $d$  in case 1 and fixed  $f = 2.0$ , and (b) the corresponding absorbed energy with respect to the cubic power of diameter. (c)  $F$ - $s$  curves and (d)  $F$ - $t$  curves of the mirrored CMMs with different enlarge factors  $f$  in case 2 and fixed  $d = 1.0 \text{ mm}$ .

**3.3.3. Effect of gradient design.** To elucidate the structure-property relationships of the lattice-based CMMs under the design framework, the properties of the gradient design were further investigated. Similar to the helix design, Fig. 17 illustrates the mechanical property indicators of interest under impact response. The unified chirality (UC) is compared with the one with radial gradient (UC-GR), and with radial and axial gradients (UC-GRA and UC-NGRA), consistent with Fig. 4. The gradient coefficients  $\zeta_r$  and  $\zeta_a$  are set as introduced in Section 2.2. Combined with the helix design, the CMMs samples with helical shape or fillet-only characteristics are applied to the gradient design, denoted as -H or -F respectively. Without loss of generality, the CMMs were set as  $d = 1 \text{ mm}$ .

The results in Fig. 17 show that although the values of the gradient coefficients are technically set, all of the demonstrated gradient designs (UC-GR, UC-GRA, and UC-NGRA) have been improved in the compressive-resist performance over the original ones. Further in terms of compressive stiffness, compressive forces, and densification strain, the bi-directional gradient designs are not always higher or lower in the values than the radial gradient designs, but the absorbed energy and specific absorbed energy of UC-GRA and UC-NGRA are better than that of UC-GR. Also, the difference in the performance of UC-GRA and UC-NGRA reflects the importance of the orientation of the axial gradient for axial impact. Overall, UC-NGRA has the best energy absorption performance, with a smaller modulus indicating its compliance and the highest twisting angle enabling the advantages of compression-to-torsion deformation. This suggests

that simultaneously shortening and widening the layers from top to bottom is a design that is consistent with the characteristics of uniaxial medium-strain-rates compression set in this paper. And it should be noted that the gradient coefficients used here have not been proven to be the optimal solution for the gradient design, which needs to be realized in the next work. However, the results have clarified the feasibility of bi-directional gradient design in the framework of energy absorption-oriented design.

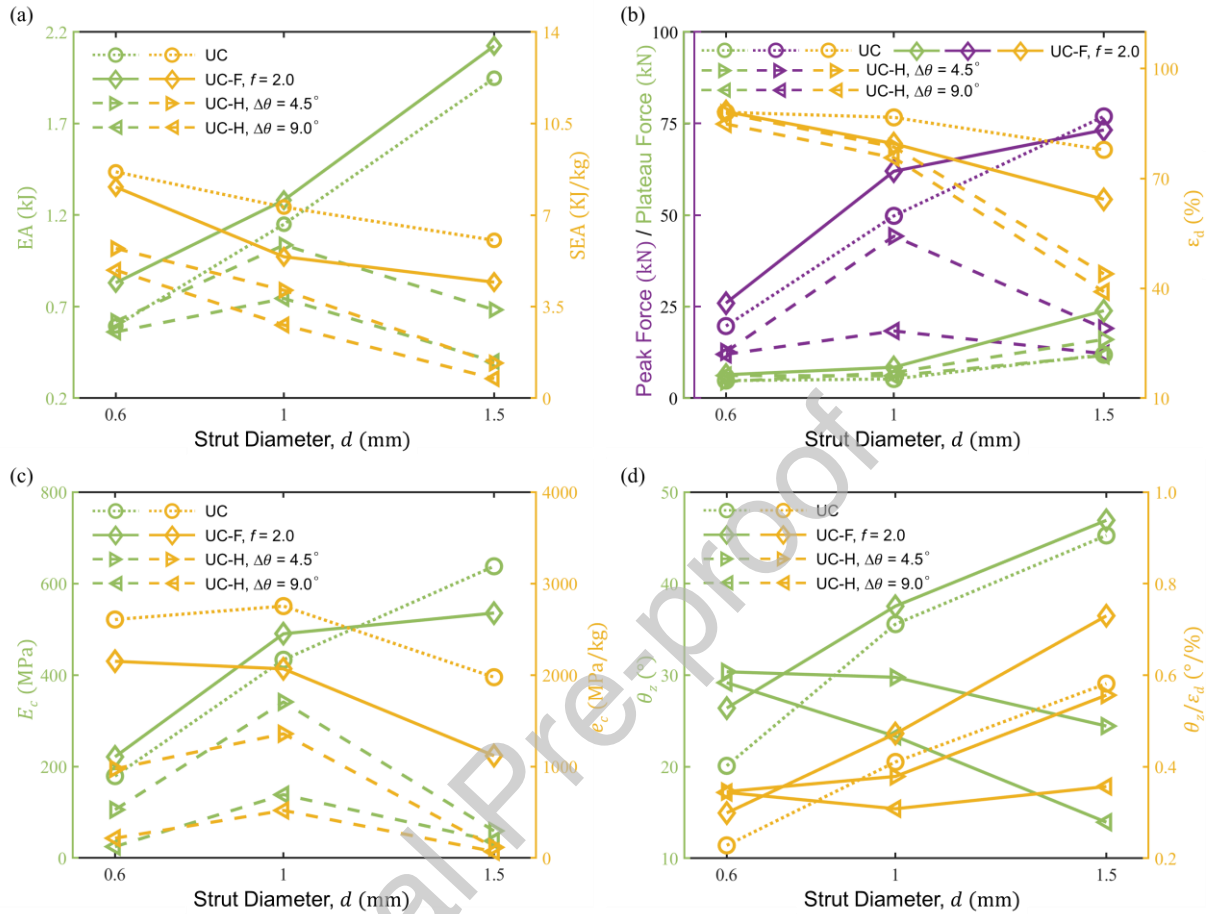


**Fig. 16. The properties of various unified chirality (UC) variants of the proposed CMMs design.** UC, UC-F, and UC-H represent the unified CMMs without fillet, with fillet, and with fillet and helix design, respectively. Nine indicators with respect to the strut diameter are shown, including (a) energy absorption EA and specific energy absorption SEA, (b) the first peak force  $F_{pk}$ , average yield plateau force  $F_{pl}$ , and densification strain  $\varepsilon_d$ , (c) compressive modulus  $E_c$  and specific compressive modulus  $e_c$ , and (d) twisting angle at densification  $\theta_z$  and twisting angle per axial strain at densification  $\theta_z/\varepsilon_d$ .

### 3.4. Energy absorption of chiral mechanical metamaterials

From the deformation mechanism analyzed in Section 3.2, it can be concluded that the lattice-based CMMs absorbs the kinetic energy of the impact load mainly through plastic deformation and frictional dissipation of the rod components, which is consistent with the conclusions from previous research [27]. And in this study, it can be found that, generally, chiral configurations determine the deformation patterns, while the shape and size of the geometry influence the magnitude of energy absorption.

The absorbed energy of the mirrored, mixed, and achiral configurations presented in Section 3.2 was calculated. As shown in Fig. 11(c), Fig. 12(c), and Fig. 13(c), the SEA of the three configurations calculated is 5.619 kJ/kg, 6.161 kJ/kg, and 6.317 kJ/kg respectively. All with assembly matrix of  $\sum c_{k,z} = 0$ , there is an 11.0 % differences in SEA between the specific stochastic achiral configuration and the mirrored chiral configuration, and a 2.4 % differences in SEA between the achiral and the mixed configurations. Considering the high nonlinearity and dispersion of the dynamic test, it can be assumed that the absorption energies of the three are roughly comparable and the performances are consistent. As mentioned before, although the chirality of the three configurations is different, the diameter and inclination of the diagonal struts are the same. And the similar  $\alpha_z$ , i.e., overall chirality (OC), indicates their similar strut orientations and thus similar plastic dissipation in energy during compressive deformation. The equivalent SEA of

mirrored, mixed, and achiral CMMs can also be suggested from the force-time ( $F-t$ ) curves in case 2 as shown in Fig. A2 in Appendix A, where they all stop the rigid wall at the same tendency.

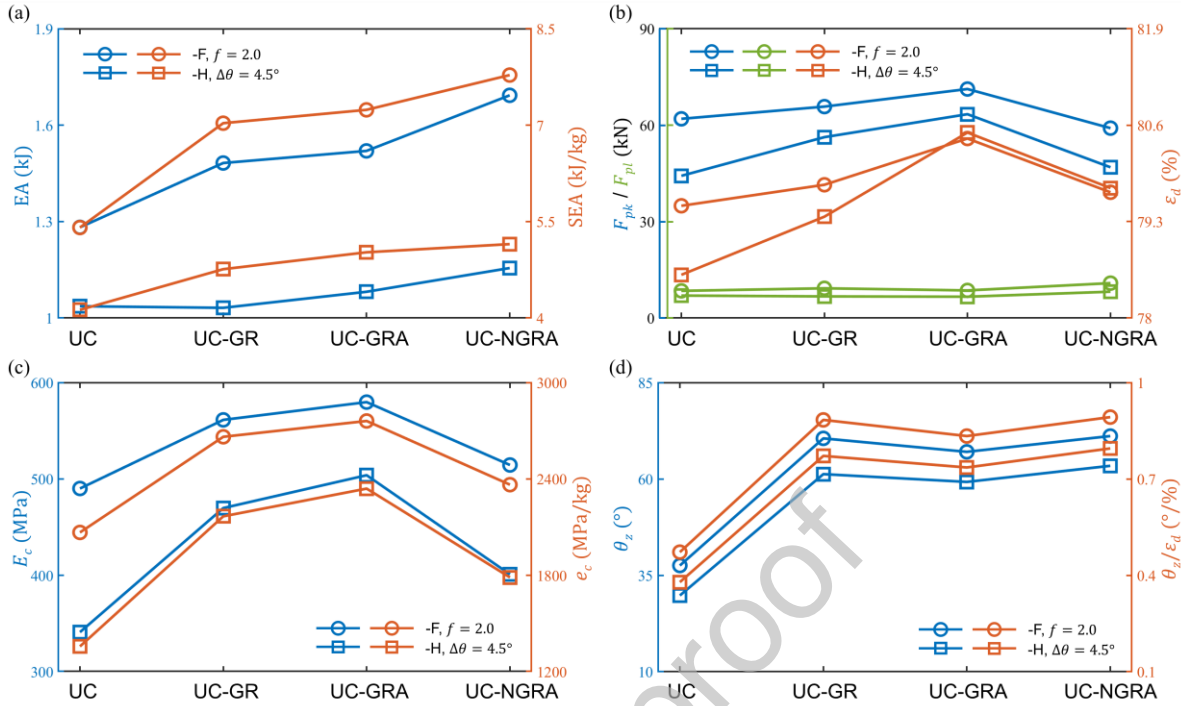


**Fig. 17. The properties of unified chirality (UC) by gradient design.** UC, UC-GR, UC-GRA, and UC-NGRA represent the unified CMMs without gradient, with  $\zeta_r = 0.930$ , with  $\zeta_r = 0.930$ ,  $\zeta_a = 0.928$ , and with  $\zeta_a = 0.930$ ,  $\zeta_a = -0.928$ , respectively. Nine indicators with respect to the designs are shown, including (a) energy absorption EA and specific energy absorption SEA, (b) the first peak force  $F_{pk}$ , average yield plateau force  $F_{pl}$ , and densification strain  $\varepsilon_d$ , (c) compressive modulus  $E_c$  and specific compressive modulus  $e_c$ , and (d) twisting angle at densification  $\theta_z$  and twisting angle per axial strain at densification  $\theta_z/\varepsilon_d$ . The legend “-F” represents the fillet-only design and “-H” means the helix design with fillet joints.

Based on the insights, the energy absorption of the lattice-based CMMs can be regulated by varying the dimensions of the unit cell through various designs as introduced in the framework. In addition to the joint-enhanced design that can generally improve mechanical properties, the helix and gradient designs actually do nothing more than adjust the orientation and diameter (aspect ratio) of the strut components, which can be characterized by  $\alpha_3$  and  $d$  respectively according to Eq. (16) and Fig. 8. Furthermore, it shows a direct linear negative correlation about the SEA and  $\alpha_3$  using UC-S samples, as illustrated in Fig. 18. It is also observed that the smaller the diameter, the higher the specific energy absorption, which is consistent with the previous discussion on material utilization.

The results demonstrate a significant improvement in the impact energy absorption performance of the designed CMMs. Using the achiral configuration with slimmed vertical struts as a counterpart (Fig. 14), the various design variants of UC are higher in both EA and SEA, as illustrated in Fig. 19. On the one hand, this confirms that chiral mechanics metamaterials can absorb more energy from external impacts due to the twist effects. On the other hand, it shows the superiority of the bi-directional gradient design, by which UC-NGRA-S increases both EA and SEA by more than 50 %, and is comparable to the total absorbed energy of UC even with a lighter mass.

The presented framework for lattice-based CMMs in this paper is based on the modulation of rod components instead of unit cells, which can realize a higher degree of design freedom and versatility than the existing methods. For illustration, a comparison with representative energy-absorbing designs of mechanical metamaterials [28,65-70] was also conducted, focusing on the energy-absorbing performance of the designed metamaterial and the flexibility and generalizability of the method. From the assessment of various designs as shown in Fig. A3 (Appendix A.8.), it can be indicated that the present method has higher SEA than existing chiral designs, has greater design space than the periodic methods, and possesses better versatility and manufacturability than the graded designs in literature. Moreover, the comprehensive parameterization makes it efficient to design and model large metamaterial systems.

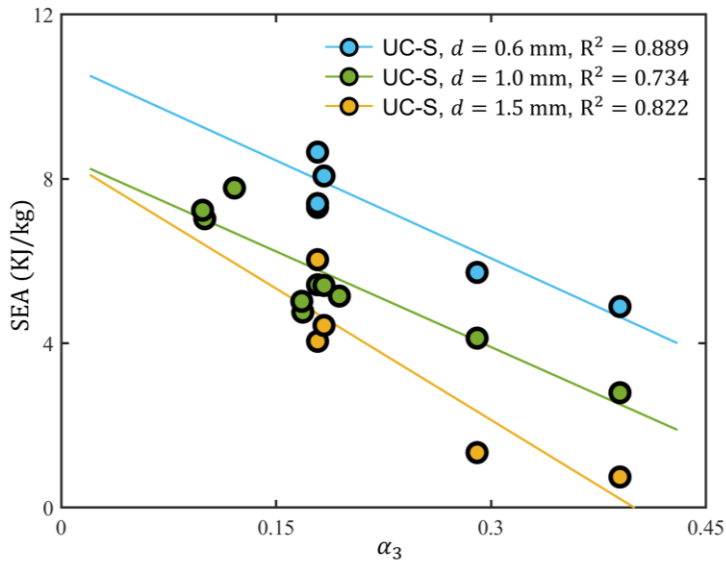


**Fig. 18.** The SEA with respect to  $\alpha_3$  of the proposed UC-S CMMs.  $f = 2.0$  and  $f_{jv} = 0.6$ , with R-squared value of the linear fit marked at each rod diameter level.

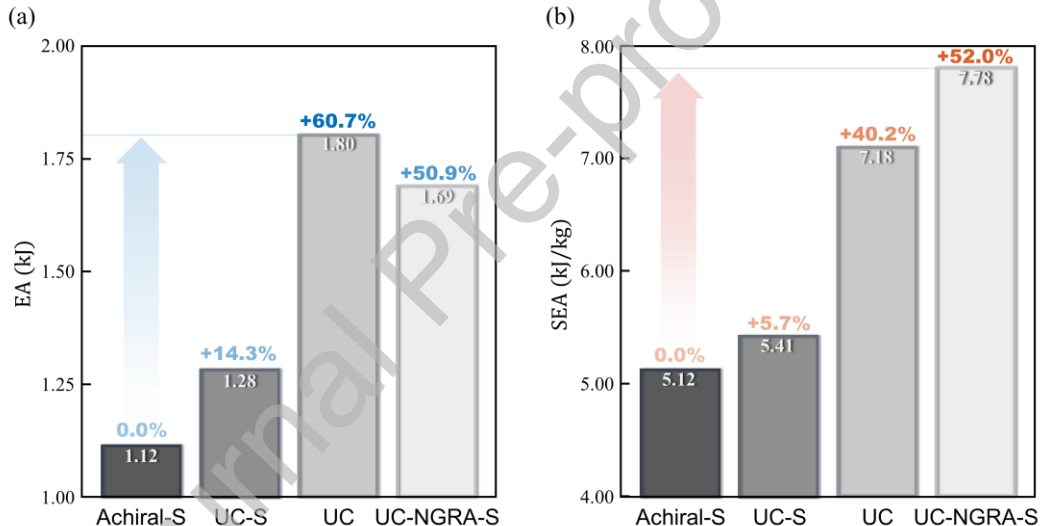


**Fig. 19.** The improvement of (a) EA and (b) SEA by chiral mechanical metamaterials.

#### 4. Conclusions

In response to the limitations of periodic design of chiral mechanical metamaterials, the constraints of additive manufacturing, and the necessity of research on the dynamic energy absorption properties of CMMs, this paper proposed a flexible framework for the design and modeling of lattice-based CMMs. This work first formed a “seeding, connecting, and enhancing” design procedure considering support-free AM, by which the scalable twist effect was enabled generally for CMMs. Then, the rigidity-theory-based joint-enhanced design, bio-inspired helix design, and bi-directional gradient design were introduced to generate variants of given chirality. Through experiment and corresponding simulation of medium-strain-rate compression, samples were designed, manufactured, and tested to obtain the mechanical responses of CMMs. the chiral features were characterized, the underlying deformation mechanism was elucidated, and the effects of various designs on the impact behavior were clarified. Finally, the energy absorption and mechanical properties were measured and analyzed, through which the following conclusions can be drawn:

- (1) Assembled by individual-defined rod components, the lattice-based CMMs is enabled to vary from periodic to aperiodic, from uniform to graded, and from ordered (chiral) to disordered (achiral). According to the proposed screw-theory-based assembly criteria, CMMs macrostructures with chiral and achiral configurations can be generated and characterized under the same framework.

- (2) The dynamically compressed CMMs samples with distinguished chirality differ in deformation process and the final shape, which, however, can be interpreted by the same deformation mechanism underlying the densification of layers. The compression-to-torsion coupling of twist effects contributes to the impact-resist performance of CMMs by absorbing more energy than achiral lattices mainly in the form of plastic deformation and friction dissipation.
- (3) The mechanical behaviors of CMMs under uniaxial impact loading is inherently determined by the diameter and orientation of the struts and the geometry of the joints, and by the shape and size of the macrostructure which is stacked layer by layer. Besides the compliance of metamaterial brought by the slimmed strut, a positive proportional relationship between EA and the cubic power of strut diameter  $d^3$ , and a negative linear relationship between SEA and chiral indicator  $\alpha_3$  are derived.
- (4) The gradient design outstands in the energy absorption compared with the original and the achiral configurations of CMMs. Simultaneously shortening and widening the layers from top to bottom is consistent with the characteristics of uniaxial impact, which along with the twist effects of CMMs and the fillet-enhanced joint design attributes to the strengthening of the compressive stability and toughness. The bi-directional graded CMMs with both radial and axial gradients exhibit an improvement in EA by 50.9 % and SEA by 52.0 %, indicating an effective design method for lattice-based metamaterials.

In this work, the proposed design framework is both comprehensive in design space and general for various lattice-based mechanical metamaterials. The results not only deepen our understanding of the mechanism of CMMs during dynamic compression, but also provide a new paradigm for the crashworthiness design of lightweight materials and structures. The presented CMMs can be adopted as filler in cushioning sandwich structures, crush boxes, and bulkheads, which will contribute to their further applications in the fields of automobiles, civil engineering, aerospace, etc. Future work may include the functional graded optimization (FGO) of CMMs, theoretical investigation on the energy absorption structure-property relationship of CMMs, and the application research by more categories of chiral mechanical metamaterials or more complex macroscopic shapes.

## Appendix A

### A.1. Physical parameters of 316L and process parameters of SLM

According to the SLM manufacturer, the chemical composition and physical parameters of SLM 316L are shown in Table A1 and Table A2 respectively. And the AM process parameters were technically set according to the process parameter database from the equipment manufacturer, as shown in Table A3. To release thermal stress, all samples were heat-treated in accordance to ASTM F3301-18a to a maximum temperature of 300 °C, held constant for 2 hours, and acclimated back to room temperature in the air.

**Table A1.** Chemical composition of SLM 316L stainless steel (wt. %).

Material	%Si	%Mn	%Ni	%Cr	%Mo	%P	%Fe
316L SS	0.423	0.218	13.251	17.204	2.178	0.012	Balance

**Table A2.** Physical parameters of SLM 316L stainless steel.

Measurement	Value
Yield stress (MPa)	470
Tensile strength (MPa)	570
Elongation at break (%)	> 15
Young's modulus (GPa)	≈ 200
Thermal conductivity (kW/K)	≈ 15
Density (kg/m <sup>3</sup> )	7.98 × 10 <sup>3</sup>
Toughness (HRC)	20

**Table A3.** Process parameters set up of SLM.

Parameter	Value
Laser thickness (μm)	30
Hatch distance (μm)	80
Laser speed (mm/s)	1200
Laser power (W)	270
Beam offset (μm)	20
Stripe width (mm)	5
Overlap (μm)	50

### A.2. Rigidity theory analysis of joint-enhanced CMMs

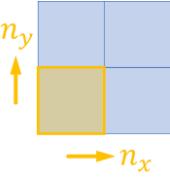
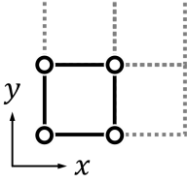
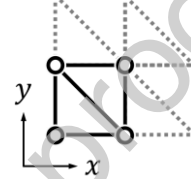
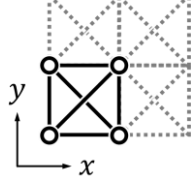
Rigidity theory is utilized to study the stability of mechanical trusses by reducing complex networks (such as lattices) to nodes constrained by rods [60,61]. The internal degrees of freedom (DOF) of a general metamaterials network provides the insights to investigate the corresponding macroscopic properties [26], which can be obtained by

$$F = 3N - N_c - M_{eq} \quad (\text{A1})$$

where  $N$ ,  $N_c$ , and  $M_{eq}$  stand for the number of nodes, constraints, and equations of equilibrium, respectively.  $M_{eq} = 3$  in 2D and equals 6 in 3D.

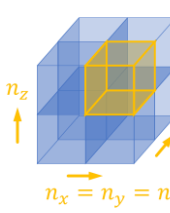
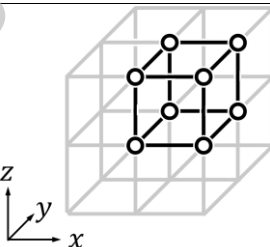
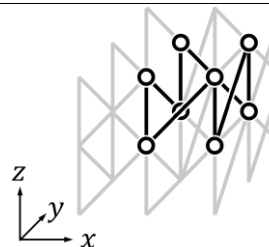
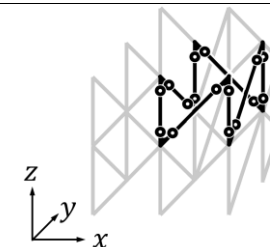
Referring to Eq. (A1), the flexibility of CMMs increased by the fillet enhanced-joints was demonstrated. First, from the typical 2D lattices cases, the DOF with respect to the numbers of unit cells in the two principal directions can be derived, as shown in Table A4. According to the DOF of their unit cell, the lattices can be classified as flexible ( $F|_{n=1} < 0$ ), isostatic ( $F|_{n=1} = 0$ ), and stressed-rigid ( $F|_{n=1} > 0$ ). It can be found that the flexible lattices gain more DOF whereas the other two lose more as the unit-cell numbers increase. The partial derivative of  $F$  with respect to the number  $n_x$  or  $n_y$  indicates the magnitude of the corresponding increase/decrease.

**Table A4.** DOF analysis of 2D lattices systems.

Configurations	Flexible ( $F _{n=1} < 0$ )	Isostatic ( $F _{n=1} = 0$ )	Stressed-rigid ( $F _{n=1} > 0$ )
			
$F$	$n_x + n_y - 1$	$n_x + n_y - n_x n_y - 1$	$n_x + n_y - 2n_x n_y - 1$
$\partial F / \partial n_x$	1	$1 - n_y$	$1 - 2n_y$
$\partial F / \partial n_y$	1	$1 - n_x$	$1 - 2n_x$

Flexible lattices tend to be bend-dominated in deformation and thus have relatively lower modulus, which is ideal for energy absorption [26]. Similar analysis can be conducted in the 3D metamaterial systems. Here,  $n_x = n_y = n$  as the radial number and  $n_z$  is the axial number due to the assembly features of the proposed CMMs. The instant PRBM of traditional cubic lattices, and the proposed Z-shaped CMMs with and without fillet are shown in Table A5. And with more materials piled up at the enhanced joints, the bending or buckling of the struts with fillet joints tend to happen in the positions offset from the joints, causing a different modeling of PRBM from the original CMMs.

**Table A5.** DOF analysis of 3D metamaterials systems.

Configurations	Cubic Lattice	Z-shaped CMMs	Z-shaped CMMs with Fillet
			
$F$	$n^2 + 2nn_z + 4n + 2n_z - 3$	$3n^2 + 2nn_z + 6n + 2n_z - 3$	$3n^2n_z + 6n^2 + 8nn_z + 4n + 5n_z$
$\partial F / \partial n$	$4 + 2n + 2n_z$	$6 + 6n + 2n_z$	$4 + 12n + 8n_z + 6nn_z$
$\partial F / \partial n_z$	$2 + 2n$	$2 + 2n$	$5 + 8n + 3n^2$

The obtained DOF and its partial derivative exhibit a linear increase along the axial direction and a quadratic increase along the radial direction of the cubic lattice, and the Z-shaped CMMs which is composed of vertical and diagonal struts is comparable to the cubic lattice on the order of magnitude of  $F$ ,  $\partial F / \partial n$ , and  $\partial F / \partial n_z$ . This indicates that the proposed original CMMs is as flexible as traditional bend-dominated lattice.

Even better, as for the CMMs with fillet, there exists a cubic term in  $F$  and a quadratic term in  $\partial F / \partial n$  and  $\partial F / \partial n_z$  with respect to the unit-cell number, which greatly improves the overall increase in DOF of 3D metamaterials systems. Therefore, the rigidity-theory-analysis demonstrates the feasibility of CMMs with joint-enhanced design.

### A.3. Johnson-Cook constitutive model of 316L

In this paper, the 3D-printed stainless steel AISI 316L was applied to construct the chiral mechanical metamaterials. Considering the large deformation and high strain rate of the impact process, Johnson-Cook (J-C) constitutive model was used to characterize the mechanical behavior of 316L. The J-C plasticity model describes the plastic behavior of materials where the yield stress is determined by the strain, the strain rate, and the temperature. The general formula [71] is

$$\sigma = \left[ A + B(\bar{\varepsilon}^{pl})^n \right] \left[ 1 + C \ln \left( \frac{\dot{\varepsilon}^{pl}}{\dot{\varepsilon}_0} \right) \right] \left[ 1 - \left( \frac{T - T_0}{T_M - T_0} \right)^m \right] \quad (\text{A2})$$

where  $\sigma$  is the equivalent plastic stress,  $\bar{\varepsilon}^{pl}$  is the equivalent plastic strain, and  $\dot{\varepsilon}^{pl}$  and  $\dot{\varepsilon}_0$  are the strain rate and the reference strain rate respectively.  $A$ ,  $B$ ,  $C$ ,  $n$ , and  $m$  are the constants of J-C model, which respectively represents the initial yield stress, hardening modulus, strain rate constant, hardening exponent, and thermal softening exponent. Without temperature effect taken into account, Eq. (A2) can be simplified as follows:

$$\sigma = \left[ A + B(\bar{\varepsilon}^{pl})^n \right] \left[ 1 + C \ln \left( \frac{\dot{\varepsilon}^{pl}}{\dot{\varepsilon}_0} \right) \right] \quad (\text{A3})$$

The J-C failure model without temperature effect is then expressed as [62]

$$\varepsilon_f = [D_1 + D_2 \exp(D_3 \eta)] [1 + D_4 \ln(\dot{\varepsilon}_p^*)] \quad (\text{A4})$$

where  $\dot{\varepsilon}_p^* = \dot{\varepsilon}^{pl} / \dot{\varepsilon}_0$ ,  $\eta$  is the triaxiality, and  $D_1$ ,  $D_2$ ,  $D_3$ , and  $D_4$  are the failure constants. The constants in the plasticity model and failure model can be measured and calculated through a series of tests with different test samples at different loads and strain rates, which has been systematically studied in literatures. The constants adopted in this work were listed in Table A6 [71,72].

**Table A6.** Constants of the 316L J-C constitutive model ( $\dot{\varepsilon}_0 = 0.001 \text{ s}^{-1}$ ).

$A(\text{MPa})$	$B(\text{MPa})$	$n$	$C$	$D_1$	$D_2$	$D_3$	$D_4$
554.05	3919.72	1.17	0.0118	0.4	120	-15	-0.025

The energy damage evolution was defined to characterize the failure after the initiation of damage, which can be described as:

$$D = \int \frac{dG_f}{G_{fc}(\theta, \bar{\varepsilon}^{pl})} = 1$$

$$G_f = \int_{\bar{\varepsilon}_0^{pl}}^{\bar{\varepsilon}_f^{pl}} L\sigma d\bar{\varepsilon}^{pl} \quad (\text{A5})$$

### A.4. Mesh convergence analysis of FEA

To determine the appropriate mesh size of FEA models, the convergence analysis was conducted using UC CMMs. The material properties, interaction, boundary condition, element types, and steps set up were the same as described in Section 2.3. The first peak force was extracted. As illustrated in Fig. A1, it showed a tendency of convergence when the element size was smaller than 0.6 mm. Thus, we chose an approximate global size of 0.5 mm to balance the accuracy and efficiency in FEA.

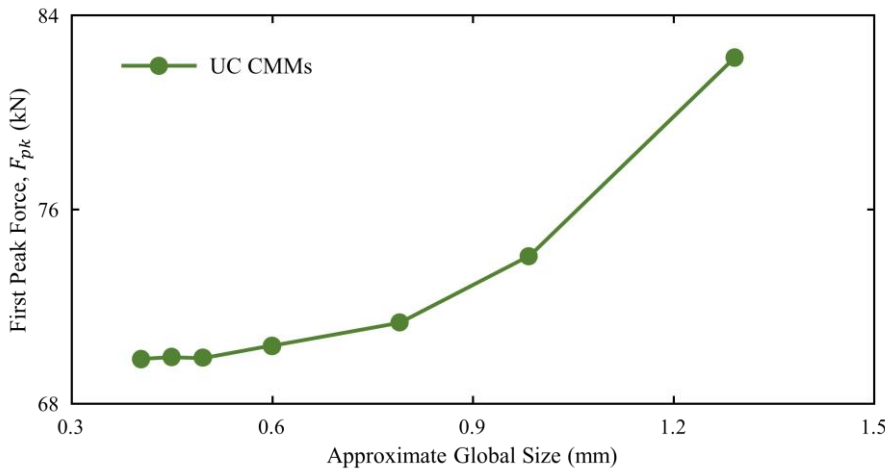


**Fig. A1.** The convergence analysis of element size.

#### A.5. Coordinate transformation of nodes for meshing

As shown in Fig. 6(c), the nodes within a cross-section of strut are firstly defined in a local coordinate and then mapped into the global coordinate based on the position and orientation of the strut, which is described by  $(\mathbf{r}, \theta, \omega)$ . The corresponding coordinate transformation can be expressed as follows:

$$[x' \ y' \ z' \ 1]^T = \mathbf{T} \cdot [x \ y \ z \ 1]^T \quad (\text{A6})$$

where  $(x, y, z)$  and  $(x', y', z')$  are the local and global coordinates of arbitrary node respectively. And the transformation matrix is obtained as:

$$\begin{aligned} \mathbf{T} &= \mathbf{T}_r(\mathbf{r}) \cdot \mathbf{R}_z(-\omega) \cdot \mathbf{R}_x(-\theta) \\ \mathbf{T}_r(\mathbf{r}) &= \begin{bmatrix} 1 & 0 & 0 & dx \\ 0 & 1 & 0 & dy \\ 0 & 0 & 1 & dz \\ 0 & 0 & 0 & 1 \end{bmatrix} \\ \mathbf{R}_x(\varphi) &= \begin{bmatrix} 1 & 0 & 0 & 0 \\ 0 & \cos \varphi & -\sin \varphi & 0 \\ 0 & \sin \varphi & \cos \varphi & 0 \\ 0 & 0 & 0 & 1 \end{bmatrix} \\ \mathbf{R}_z(\varphi) &= \begin{bmatrix} \cos \varphi & -\sin \varphi & 0 & 0 \\ \sin \varphi & \cos \varphi & 0 & 0 \\ 0 & 0 & 1 & 0 \\ 0 & 0 & 0 & 1 \end{bmatrix} \end{aligned} \quad (\text{A7})$$

Then, the wedge elements can be defined by matching the nodes between adjacent cross-section.

#### A.6. Characterization of chirality using OC, DC, and CC

In this work, the chiral geometry of CMMs was evaluated by mathematically describing the overall chirality, deviation of chirality, and the consistency of chirality between layers, which can be referred to as OC, DC, and CC respectively. OC is defined as illustrated in Section 3.1. Analogy to the concept of variance in statistics, DC describes the deviation of chirality of each layer with the overall chirality, expressed as

$$\begin{aligned} \beta_z &= \frac{1}{N_z} \sum (c_{k,z} - c)^2 \\ c &= \frac{1}{N_z} \sum c_{k,z} \\ \beta_z &\in [0, +1] \end{aligned} \quad (\text{A8})$$

Referring to Eq. (A8), the bigger DC, the higher deviation. Meanwhile, CC describes the consistency of chirality in adjacent layers as:

$$\begin{aligned} \gamma_z &= \prod e^{-\frac{|c_{k,z} - c_{k+1,z}|}{N_z}} \\ \gamma_z &\in [0, +1] \end{aligned} \quad (\text{A9})$$

Eq. (A9) indicates that the CMMs with good consistency has a  $\gamma_z$  close to 1. Following that, the characterizations of the representative configurations are listed in Table A7.

**Table A7.** Characterization of the chirality of the proposed CMMs.

Configurations	Overall chirality (OC), $\alpha_z$	DC, $\beta_z$	CC, $\gamma_z$
Unified	$\begin{bmatrix} 0.4105 & & \\ & 0.4105 & \\ & & 0.1789 \end{bmatrix}$	0.0000	1.0000
Mirrored	$\begin{bmatrix} 0.4105 & & \\ & 0.4105 & \\ & & 0.1789 \end{bmatrix}$	1.0000	0.8187
Mixed	$\begin{bmatrix} 0.4105 & & \\ & 0.4105 & \\ & & 0.1789 \end{bmatrix}$	1.0000	0.4493
Achiral	$\begin{bmatrix} 0.4127 & 0.0028 & 0.0065 \\ 0.0028 & 0.4096 & 0.0035 \\ 0.0065 & 0.0035 & 0.1777 \end{bmatrix}$	0.0091	0.9089

It can tell from the table that the four CMMs have close or even the same OC. All with  $\sum c_{k,z} = 0$ , the left/right handedness in each layer of mirrored or mixed type has a serious deviation indicated by DC, while the achiral CMMs is literally achiral everywhere. Moreover, CC of the mirrored CMMs is bigger than that of the mixed one, implying that there exist more changes of layer handedness in the latter configuration.

#### A.7. Force-time curves of various CMMs configurations

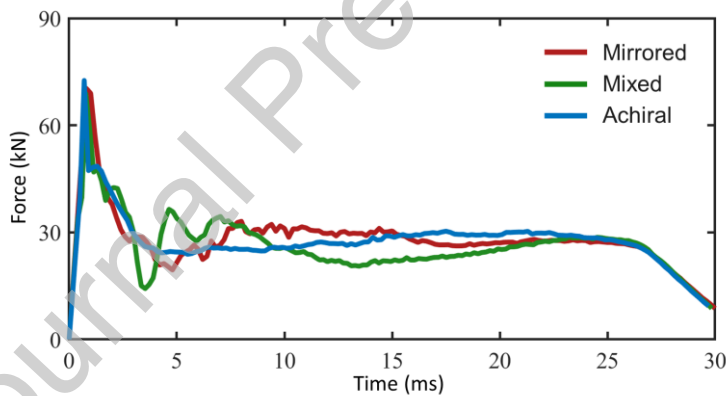


**Fig. A2.** The force-time curves of the mirrored, mixed, and achiral CMMs under case 2. It laterally indicates that the chiral geometrical features contribute to the energy absorption of the CMMs in a comparable way.

#### A.8. Comparison between various energy-absorbing designs

As illustrated in Fig. A3, a comparison with recent-reported representative energy-absorbing designs of mechanical metamaterials [28,65-70] was conducted, focusing on the energy-absorbing performance of the designed metamaterial and the flexibility and generalizability of the method. Specifically, the values of indicators are either extracted or calculated, including the EA, the SEA, the densification strain representing the range of collapse displacement, the relative density representing the lightweight degree, and the dimensions of design parameters representing the design flexibility. For a fair and clear illustration, the corresponding numerical values were mapped to rankings with the highest value ranked as 1. Here the rank of relative density is reversed because a lighter weight is more desired for lightweight material and structure design. What's more, the generalizability of the methods is also ranked under the consideration of manufacturability and the feasibility of applying to other designs. In this way, the design method that forms the largest envelope area in the six-dimensional ranking chart in Fig. 20 indicates the best overall performance.

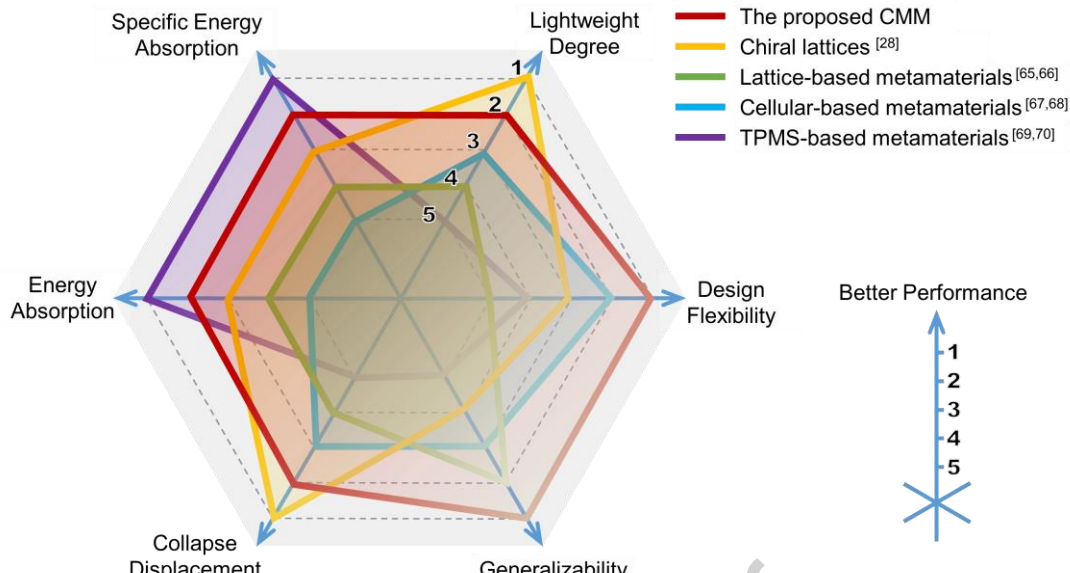


**Fig. A3. A six-dimensional ranking comparison between energy-absorbing designs of mechanical metamaterials.** Representative designs of chiral, lattice-based, cellular-based, and TPMS-based mechanical metamaterials are illustrated.

It is worth pointing out that due to the specific constituent materials and structural parameters of the designed metamaterials are different, and not all of the mechanical properties have been optimized accordingly, the comparative ranking inevitably has subjectivity. However, inspirations can be drawn from this. Despite the higher EA and SEA of TPMS-based design, manufacturing constraints make it difficult to reduce the mass further, and the type of unit cells is more limited. The existing methods can be categorized into periodic and aperiodic in terms of arrangement characteristics, while gradient design is one of most common approach to achieve aperiodicity. The periodic method in literature is more mature, but the design freedom is limited due to the repetitive arrangement of unit cell with given pattern. The gradient design by varying the relative density in space can significantly improve the mechanical properties and energy-absorbing effect of metamaterials, but it is also faced with the problem of method versatility. In contrast, the present method is no longer limited to the definition of unit-cell forms and thus has higher design flexibility and higher generalizability for lattice-based metamaterials. Moreover, the comprehensive parameterization makes it efficient to design and model large metamaterial systems.

#### CRediT authorship contribution statement

**Weiyun Xu:** Conceptualization, Methodology, Writing- Original draft preparation. **Chang Zhou:** Software, Writing- Reviewing and Editing. **Hanyu Zhang:** Visualization. Writing- Reviewing and Editing. **Zhao Liu:** Data curation. **Ping Zhu:** Investigation. Supervision.

#### Competing interests

The authors declare no competing interests.

#### Acknowledgments

This work was sponsored by Natural Science Foundation of Shanghai (Grant No. 21ZR1431500 and No. 23ZR1431600).

#### Data availability

Data will be made available on request.

#### References

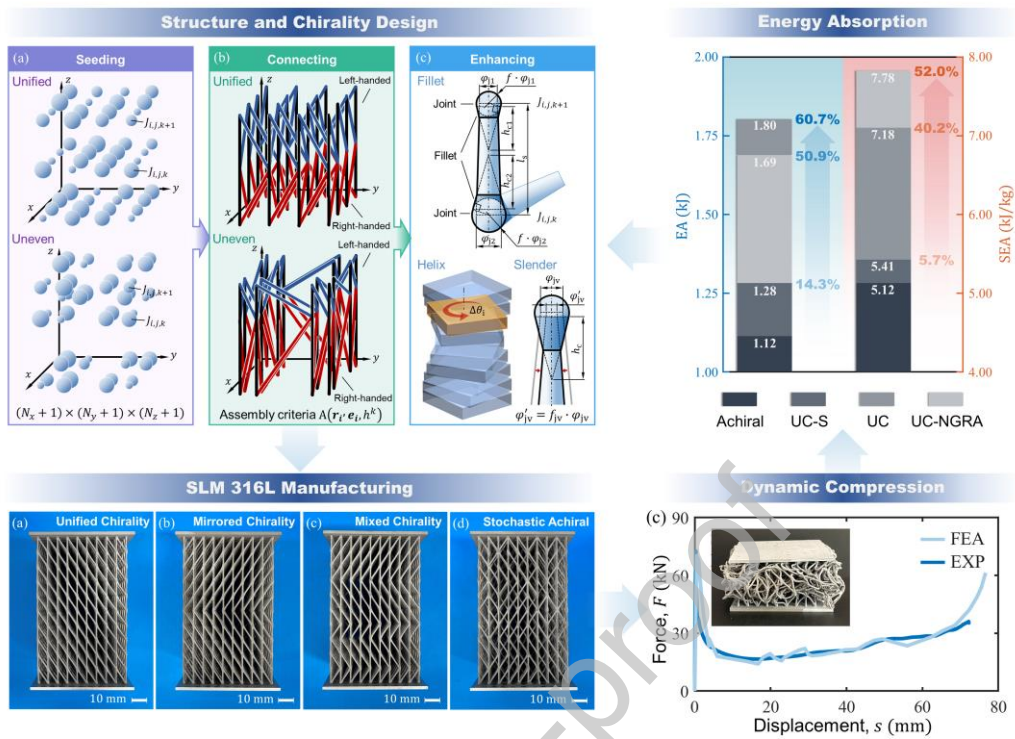
- [1] Ha N S and Lu G. A review of recent research on bio-inspired structures and materials for energy absorption applications. *Compos. Pt. B-Eng.* **181**, 107496 (2020). <https://doi.org/10.1016/j.compositesb.2019.107496>

- [2] Pan F et al. 3D pixel mechanical metamaterials. *Adv. Mater.* **31**, 1900548 (2019). <https://doi.org:10.1002/adma.201900548>
- [3] Bertoldi K, Vitelli V, Christensen J and Van Hecke M. Flexible mechanical metamaterials. *Nat. Rev. Mater.* **2**, 17066 (2017). <https://doi.org:10.1038/natrevmats.2017.66>
- [4] Yuan S, Chua C K and Zhou K. 3D-printed mechanical metamaterials with high energy absorption. *Adv. Mater. Technol.* **4** (2018). <https://doi.org:10.1002/admt.201800419>
- [5] Sharma D and Hiremath S S. Bio-inspired repeatable lattice structures for energy absorption: Experimental and finite element study. *Compos. Struct.* **283**, 115102 (2022). <https://doi.org:https://doi.org/10.1016/j.compstruct.2021.115102>
- [6] Wang J, Luo X, Wang K, Yao S and Peng Y. On impact behaviors of 3D concave structures with negative Poisson's ratio. *Compos. Struct.* **298** (2022). <https://doi.org:10.1016/j.compstruct.2022.115999>
- [7] Fu J et al. Isotropic design and mechanical characterization of TPMS-based hollow cellular structures. *Compos. Struct.* **279** (2022). <https://doi.org:10.1016/j.compstruct.2021.114818>
- [8] Siddique S H, Hazell P J, Wang H, Escobedo J P and Ameri A A. H. Lessons from nature: 3D printed bio-inspired porous structures for impact energy absorption - A review. *Addit. Manuf.* **58**, 103051 (2022). <https://doi.org:https://doi.org/10.1016/j.addma.2022.103051>
- [9] Jiao P. Mechanical energy metamaterials in interstellar travel. *Prog. Mater. Sci.* **137**, 101132 (2023). <https://doi.org:https://doi.org/10.1016/j.pmatsci.2023.101132>
- [10] Li J, Ha C S and Lakes R S. Observation of squeeze-twist coupling in a chiral 3D isotropic lattice. *Phys. Status Solidi B-Basic Solid State Phys.* (2019). <https://doi.org:10.1002/pssb.201900140>
- [11] Gao Z et al. Additive manufacture of ultrasoft bioinspired metamaterials. *Int. J. Mach. Tools Manuf.* **195**, 104101 (2024). <https://doi.org:https://doi.org/10.1016/j.ijmachtools.2023.104101>
- [12] Pham M S, Liu C, Todd I and Lertthanasant J. Damage-tolerant architected materials inspired by crystal microstructure. *Nature* **565**, 305-311 (2019). <https://doi.org:10.1038/s41586-018-0850-3>
- [13] Gao Z et al. Additively manufactured high-energy-absorption metamaterials with artificially engineered distribution of bio-inspired hierarchical microstructures. *Compos. Pt. B-Eng.* **247** (2022). <https://doi.org:10.1016/j.compositesb.2022.110345>
- [14] Frenzel T, Kadic M and Wegener M. Three-dimensional mechanical metamaterials with a twist. *Science* **358**, 1072-1074 (2017). <https://doi.org:doi:10.1126/science.aoa4640>
- [15] Kadic M, Diatta A, Frenzel T, Guenneau S and Wegener M. Static chiral Willis continuum mechanics for three-dimensional chiral mechanical metamaterials. *Phys. Rev. B* **99** (2019). <https://doi.org:10.1103/PhysRevB.99.214101>
- [16] Wang J S et al. Hierarchical chirality transfer in the growth of towel gourd tendrils. *Sci. Rep.* **3** (2013). <https://doi.org:10.1038/srep03102>
- [17] Gross P et al. Quantifying how DNA stretches, melts and changes twist under tension. *Nat. Phys.* **7**, 731-736 (2011). <https://doi.org:10.1038/nphys2002>
- [18] Liu D et al. Spider dragline silk as torsional actuator driven by humidity. *Sci. Adv.* **5**, eaau9183 (2019). <https://doi.org:10.1126/sciadv.aau9183>
- [19] Yu X, Zhou J, Liang H, Jiang Z and Wu L. Mechanical metamaterials associated with stiffness, rigidity and compressibility: A brief review. *Prog. Mater. Sci.* **94**, 114-173 (2018). <https://doi.org:https://doi.org/10.1016/j.pmatsci.2017.12.003>
- [20] Cui H et al. Design and printing of proprioceptive three-dimensional architected robotic metamaterials. *Science* **376**, 1287-1293 (2022). <https://doi.org:10.1126/science.abn0090>
- [21] Xu W, Liu Z, Wang L and Zhu P. 3D chiral metamaterial modular design with highly-tunable tension-twisting properties. *Mater. Today Commun.* **30** (2022). <https://doi.org:10.1016/j.mtcomm.2021.103006>
- [22] Frenzel T, Kopfler J, Jung E, Kadic M and Wegener M. Ultrasound experiments on acoustical activity in chiral mechanical metamaterials. *Nat. Commun.* **10**, 3384 (2019). <https://doi.org:10.1038/s41467-019-11366-8>
- [23] Eringen A C. *Microcontinuum field theories: I. Foundations and solids.* (Springer Science & Business Media, 2012).
- [24] Kaarthik P, Sanchez F L, Avtges J and Truby R L. Motorized, untethered soft robots via 3D printed auxetics. *Soft Matter* **18**, 8229-8237 (2022). <https://doi.org:10.1039/d2sm00779g>
- [25] Ye M, Gao L, Wang F and Li H. A novel design method for energy absorption property of chiral mechanical metamaterials. *Materials* **14**, 5386 (2021). <https://doi.org:10.3390/ma14185386>
- [26] Ashby M F. The properties of foams and lattices. *Philos. Trans. R. Soc. A-Math. Phys. Eng. Sci.* **364**, 15-30 (2006). <https://doi.org:10.1098/rsta.2005.1678>
- [27] Meng L et al. An emerging class of hyperbolic lattice exhibiting tunable elastic properties and impact absorption through chiral twisting. *Extreme Mech. Lett.* **40** (2020). <https://doi.org:10.1016/j.eml.2020.100869>
- [28] Xu W et al. Crushing behavior of contact-aided AlSi10Mg sandwich structure based on chiral mechanical metamaterials. *Int. J. Mech. Sci.* **260**, 108636 (2023). <https://doi.org:https://doi.org/10.1016/j.ijmecsci.2023.108636>
- [29] Yang C, Yang K, Tian Y, Fu M and Hu L. Theoretical analysis on the stiffness of compression-torsion coupling metamaterials. *Extreme Mech. Lett.* **46** (2021). <https://doi.org:10.1016/j.eml.2021.101336>

- [30] Ha C S, Plesha M E and Lakes R S. Chiral three-dimensional isotropic lattices with negative Poisson's ratio. *Phys. Status Solidi B-Basic Solid State Phys.* **253**, 1243-1251 (2016). <https://doi.org/10.1002/pssb.201600055>
- [31] Duan S Y, Xi L, Wen W B and Fang D N. A novel design method for 3D positive and negative Poisson's ratio material based on tension-twist coupling effects. *Compos. Struct.* **236**, 111899 (2020). <https://doi.org/10.1016/j.compstruct.2020.111899>
- [32] Ha C S, Plesha M E and Lakes R S. Chiral three-dimensional lattices with tunable Poisson's ratio. *Smart Mater. Struct.* **25** (2016). <https://doi.org/10.1088/0964-1726/25/5/054005>
- [33] Xu W, Wang L, Liu Z and Zhu P. General assembly rules for metamaterials with scalable twist effects. *Int. J. Mech. Sci.* **259**, 108579 (2023). <https://doi.org/10.1016/j.ijmecsci.2023.108579>
- [34] Chen Y, Frenzel T, Zhang Q, Kadic M and Wegener M. Cubic metamaterial crystal supporting broadband isotropic chiral phonons. *Phys. Rev. Mater.* **5**, 025201 (2021). <https://doi.org/10.1103/PhysRevMaterials.5.025201>
- [35] Li X, Yang Z and Lu Z. Design 3D metamaterials with compression-induced-twisting characteristics using shear-compression coupling effects. *Extreme Mech. Lett.* **29** (2019). <https://doi.org/10.1016/j.eml.2019.100471>
- [36] Lipton J I et al. Handedness in shearing auxetics creates rigid and compliant structures. *Science* **360**, 632-635 (2018). <https://doi.org/10.1126/science.aar4586>
- [37] Fernandez-Corbaton I et al. New twists of 3D chiral metamaterials. *Adv. Mater.* **31**, 1807742 (2019). <https://doi.org/10.1002/adma.201807742>
- [38] Chen W and Huang X. Topological design of 3D chiral metamaterials based on couple-stress homogenization. *J. Mech. Phys. Solids* **131**, 372-386 (2019). <https://doi.org/10.1016/j.jmps.2019.07.014>
- [39] Jenett B et al. Discretely assembled mechanical metamaterials. *Sci. Adv.* **6**, eabc9943 (2020). <https://doi.org/10.1126/sciadv.abc9943>
- [40] Chen X, He T, Hu Y and Feng M. A 3D dislocated re-entrant structure with compression-twist coupling effect. *Smart Mater. Struct.* **32**, 055009 (2023). <https://doi.org/10.1088/1361-665X/acc621>
- [41] Zhao W, Zhu J, Liu L, Leng J and Liu Y. A bio-inspired 3D metamaterials with chirality and anti-chirality topology fabricated by 4D printing. *Int. J. Smart Nano Mater.* **14**, 1-20 (2023). <https://doi.org/10.1080/19475411.2022.2120110>
- [42] Ziemke P, Frenzel T, Wegener M and Gumbsch P. Tailoring the characteristic length scale of 3D chiral mechanical metamaterials. *Extreme Mech. Lett.* **32**, 100553 (2019). <https://doi.org/10.1016/j.eml.2019.100553>
- [43] Frenzel T et al. Large characteristic lengths in 3D chiral elastic metamaterials. *Commun. Mater.* **2** (2021). <https://doi.org/10.1038/s43246-020-00107-w>
- [44] Coulais C, Kettenis C and van Hecke M. A characteristic length scale causes anomalous size effects and boundary programmability in mechanical metamaterials. *Nat. Phys.* **14**, 40-44 (2017). <https://doi.org/10.1038/nphys4269>
- [45] Qi C., Jiang F. and Yang S. Advanced honeycomb designs for improving mechanical properties: A review. *Compos. Pt. B-Eng.* **227** (2021). <https://doi.org/10.1016/j.compositesb.2021.109393>
- [46] Xing, J. et al. Crashworthiness design and optimization of bamboo-inspired tube with gradient multi-cells. *Thin-Walled Struct.* **191**, 111034 (2023). <https://doi.org/10.1016/j.tws.2023.111034>
- [47] Ahamed M.K., Wang H. and Hazell P.J. From biology to biomimicry: Using nature to build better structures—a review. *Constr. Build. Mater.* **320**, 126195 (2022).
- [48] Yang H. et al. Mechanical properties of hierarchical lattice via strain gradient homogenization approach. *Compos. Pt. B-Eng.* **271** (2024). <https://doi.org/10.1016/j.compositesb.2023.111153>
- [49] He Q., Feng J., Chen Y. and Zhou H. Mechanical properties of spider-web hierarchical honeycombs subjected to out-of-plane impact loading, *J. Sandw. Struct. Mater.* **22** (3), 771–796 (2020).
- [50] Ghazlan A., Nguyen T., Ngo T. and Linforth S. Performance of a 3D printed cellular structure inspired by bone, *Thin-Walled Struct.* **151**, 106713 (2020).
- [51] Islam M.K., Hazell P.J., Escobedo J.P. and Wang H. Biomimetic armour design strategies for additive manufacturing: A review. *Mater. Des.* **205**, 109730 (2021).
- [52] Cheng L, Thomas A, Glancey J L and Karlsson A M. Mechanical behavior of bio-inspired laminated composites. *Compos. Pt. A-Appl. Sci. Manuf.* **42**, 211-220 (2011). <https://doi.org/10.1016/j.compositesa.2010.11.009>
- [53] Wen S M et al. Biomimetic Gradient Bouligand Structure Enhances Impact Resistance of Ceramic - Polymer Composites. *Adv. Mater.* **35** (2023). <https://doi.org/10.1002/adma.202211175>
- [54] Wang H, Li S, Liu Z, Wang Z and Li Z. Investigation on the dynamic response of circular sandwich panels with the bio-inspired gradient core. *Thin-Walled Struct.* **149** (2020). <https://doi.org/10.1016/j.tws.2020.106667>
- [55] Sun T, Yang S and Lian B, *Finite and instantaneous screw theory in robotic mechanism*. (Springer Nature, 2020).
- [56] Park S I and Rosen D W. Homogenization of mechanical properties for material extrusion periodic lattice structures considering joint stiffening effects. *J. Mech. Des.* **140**, 111414 (2018). <https://doi.org/10.1115/1.4040704>
- [57] Cao X F, Duan S Y, Liang J, Wen W B and Fang D N. Mechanical properties of an improved 3D-printed rhombic dodecahedron stainless steel lattice structure of variable cross section. *Int. J. Mech. Sci.* **145**, 53-63 (2018). <https://doi.org/10.1016/j.ijmecsci.2018.07.006>

- [58] Wang X, Zhu L, Sun L and Li N. Optimization of graded filleted lattice structures subject to yield and buckling constraints. *Mater. Des.* **206** (2021). <https://doi.org/10.1016/j.matdes.2021.109746>
- [59] Qi D et al. Mechanical behaviors of SLM additive manufactured octet-truss and truncated-octahedron lattice structures with uniform and taper beams. *Int. J. Mech. Sci.* **163**, 105091 (2019). <https://doi.org/10.1016/j.ijmecsci.2019.105091>
- [60] Thorpe M F. Continuous deformations in random networks. *J. Non-Cryst. Solids* **57**, 355-370 (1983). [https://doi.org/10.1016/0022-3093\(83\)90424-6](https://doi.org/10.1016/0022-3093(83)90424-6)
- [61] Maxwell J C. XLV. On reciprocal figures and diagrams of forces. *The London, Edinburgh, and Dublin Philosophical Magazine and Journal of Science* **27**, 250-261 (1864). <https://doi.org/10.1080/14786446408643663>
- [62] Goswami D et al. Mechanical metamaterials with programmable compression-twist coupling. *Smart Mater. Struct.* **30**, 015005 (2021). <https://doi.org/10.1088/1361-665x/abc182>
- [63] Lielens G. Micro-macro modeling of structured materials. *PhD thesis*, Université catholique de Louvain, 1999.
- [64] Ha N S and Lu G. Thin-walled corrugated structures: A review of crashworthiness designs and energy absorption characteristics. *Thin-Walled Struct.* **157**, 106995 (2020).
- [65] Gao Z et al. Data-driven design of biometric composite metamaterials with extremely recoverable and ultrahigh specific energy absorption. *Compos. Pt. B-Eng.* **251** (2023). <https://doi.org/10.1016/j.compositesb.2022.110468>
- [66] Sun Z P, Guo Y B and Shim V P W. Characterisation and modeling of additively-manufactured polymeric hybrid lattice structures for energy absorption. *Int. J. Mech. Sci.* **191** (2021). <https://doi.org/10.1016/j.ijmecsci.2020.106101>
- [67] Qi D et al. Impact energy absorption of functionally graded chiral honeycomb structures. *Extreme Mech. Lett.* **32** (2019). <https://doi.org/10.1016/j.eml.2019.100568>
- [68] Wu H, Zhang X and Liu Y. In-plane crushing behavior of density graded cross-circular honeycombs with zero Poisson's ratio. *Thin-Walled Struct.* **151** (2020). <https://doi.org/10.1016/j.tws.2020.106767>
- [69] du Plessis A et al. Properties and applications of additively manufactured metallic cellular materials: A review. *Prog. Mater. Sci.* **125**, 100918 (2022). <https://doi.org/https://doi.org/10.1016/j.pmatsci.2021.100918>
- [70] Zhang, J. et al. A study of multi-stage energy absorption characteristics of hybrid sheet TPMS lattices. *Thin-Walled Struct.* **190** (2023). <https://doi.org/10.1016/j.tws.2023.110989>
- [71] Li Y, Ge Y, Lei J and Bai W. Mechanical properties and constitutive model of selective laser melting 316L stainless steel at different scanning speeds. *Adv. Mater. Sci. Eng.* **2022**, 1-13 (2022). <https://doi.org/10.1155/2022/2905843>
- [72] Tamer Y, Toros S and Ozturk F. Numerical and experimental comparison of fractural characteristics of 316L stainless steel. *J. Mater. Eng. Perform.* **32**, 1103-1118 (2023). <https://doi.org/10.1007/s11665-022-07152-1>

## Graphical Abstract



## Author Contributions

**Weiyun Xu:** Conceptualization, Methodology, Writing- Original draft preparation. **Chang Zhou:** Software, Writing- Reviewing and Editing. **Hanyu Zhang:** Visualization. Writing- Reviewing and Editing. **Zhao Liu:** Data curation. **Ping Zhu:** Investigation. Supervision.

## Declaration of interests

- The authors declare that they have no known competing financial interests or personal relationships that could have appeared to influence the work reported in this paper.
- The authors declare the following financial interests/personal relationships which may be considered as potential competing interests:

---

Zhao Liu reports financial support was provided by Natural Science Foundation of Shanghai. If there are other authors, they declare that they have no known competing financial interests or personal relationships that could have appeared to influence the work reported in this paper.

---